Micromechanics of brittle faulting and cataclastic flow in Mount Etna basalt

Patrick Baud, Wei Zhu, Sergio Vinciguerra, Teng-Fong Wong

AGU PUBLICATIONS

JGR

Journal of Geophysical Research: Solid Earth

RESEARCH ARTICLE
10.1002/2016JB012826

Key Points:
- 65 new uniaxial and triaxial experiments on basalt from Mount Etna
- Analysis of the impact of pores, microcracks, and phenocrysts on brittle failure of basalt
- Micromechanism of inelastic compaction in basalt

Correspondence to:
P. Baud,
patrick.baud@unistra.fr

Citation:
Zhu, W., P. Baud, S. Vinciguerra, and T.-f. Wong (2016), Micromechanics of brittle faulting and cataclastic flow in Mount Etna basalt, *J. Geophys. Res. Solid Earth*, *121*, 4268–4289, doi:10.1002/2016JB012826.

Received 15 JAN 2016
Accepted 7 JUN 2016
Accepted article online 10 JUN 2016
Published online 30 JUN 2016

Micromechanics of brittle faulting and cataclastic flow in Mount Etna basalt

Wei Zhu[1], Patrick Baud[2], Sergio Vinciguerra[3], and Teng-fong Wong[1,4]

[1]Department of Geosciences, State University of New York, Stony Brook, New York, USA, [2]Institut de Physique du Globe de Strasbourg (UMR 7516 CNRS, Université de Strasbourg/EOST), Strasbourg, France, [3]Department of Earth Sciences, University of Turin, Turin, Italy, [4]Earth System Science Programme, Faculty of Science, The Chinese University of Hong Kong, Hong Kong

Abstract Understanding how the strength of volcanic rocks varies with stress state, pressure, and microstructural attributes is fundamental to understanding the dynamics and tectonics of a volcanic system and also very important in applications such as geothermics or reservoir management in volcanic environments. In this study we investigated the micromechanics of deformation and failure in basalt, focusing on samples from Mount Etna. We performed 65 uniaxial and triaxial compression experiments on nominally dry and water-saturated samples covering a porosity range between 5 and 16%, at effective pressures up to 200 MPa. Dilatancy and brittle faulting were observed in all samples with porosity of 5%. Water-saturated samples were found to be significantly weaker than comparable dry samples. Shear-enhanced compaction was observed at effective pressures as low as 80 MPa in samples of 8% porosity. Microstructural data revealed the complex interplay of microcracks, pores, and phenocrysts on dilatant failure and inelastic compaction in basalt. The micromechanics of brittle failure is controlled by wing crack propagation under triaxial compression and by pore-emanated cracking under uniaxial compression especially in the more porous samples. The mechanism of inelastic compaction in basalt is cataclastic pore-collapse in agreement with a recent dual-porosity model.

1. Introduction

Basalt is a major rock type of the crust, and its mechanical properties exert significant influence over many tectonic and volcanic processes. A systematic investigation of basalt deformation and failure mode is therefore of fundamental importance not only for understanding the dynamics of volcanic systems but also for other applications related to engineering geology [*Jiang et al.*, 2014], geothermal systems [*Ásmundsson et al.*, 2014; *Fowler et al.*, 2015; *Pope et al.*, 2015], reservoirs in volcanic environments [*Wu et al.*, 2006; *Ólvasdóttir et al.*, 2015], and CO_2 sequestration [*Matter et al.*, 2009; *Khatiwada et al.*, 2012]. Numerous studies have been conducted on the elastic and transport properties of basalts, and how they evolve with hydrostatic loading [*Vinciguerra et al.*, 2005; *Adelinet et al.*, 2010; *Fortin et al.*, 2010] and cyclic uniaxial compression [*Heap et al.*, 2009]. There have also been investigations of brittle failure and creep of relatively compact basalts [e.g., *Rocchi et al.*, 2004; *Benson et al.*, 2007; *Heap et al.*, 2011; *Violay et al.*, 2012, 2015]. For porous basalt *Shimada* [2000] conducted one of the earliest studies of the failure mode, which was followed up by *Loaiza et al.* [2012] and *Adelinet et al.* [2013], who documented a transition of failure mode from brittle faulting to cataclastic flow with increasing confinement at room temperature in basalts from the Azores and Reykjanes (Iceland), respectively. These recent studies show that the phenomenology of failure in porous basalt is qualitatively similar to that in porous siliciclastic and carbonate rocks [e.g., *Wong et al.*, 1997; *Vajdova et al.*, 2004].

Since its formation can involve relatively complex thermal histories, the porosity of a basalt may extend over a broad range. Because most of the previous rock mechanics studies of basalt are site specific and consider samples of a relatively narrow range of porosity, questions on how porosity and preexisting damage influence failure remain unresolved. In a recent study of tuff, *Zhu et al.* [2011] have demonstrated the usefulness of a systematic study of mechanical deformation and related microstructure for elucidating the roles of porosity and preexisting damage in controlling failure in this volcanic rock. Notwithstanding the similarities in the phenomenology of failure in porous sandstone, limestone, and tuff, subtle but significant differences in the micromechanical processes have been identified in this recent study, in particular about the role of micropores and microcracks on dilatancy and inelastic compaction in the different rock types. This motivated us to undertake a parallel investigation of porous basalt using a similar methodology, so as to gain a deeper

understanding of the phenomenology and micromechanics of brittle faulting and cataclastic flow of this major rock type of the oceanic crust.

Mechanical deformation was performed on six blocks of basalt samples from Mount Etna, with porosities ranging from 4.7% to 16.0%. Our samples are porphyritic alkali basalts from cores considered to be similar to those investigated earlier by *Heap et al.* [2009] and *Fortin et al.* [2010]. Uniaxial compression tests were conducted on a selection of samples from the six blocks. In addition, a series of conventional triaxial compression tests were performed on samples selected from four of the six blocks at different confining pressures under both saturated and nominal dry conditions. Previous investigations on Etna basalt have reached apparently contradictory conclusions regarding the effect of water on its strength. Whereas *Heap* [2009] reported significant weakening in the presence of water, *Fortin et al.* [2010] observed an almost negligible effect. To probe this question deeper, we also conducted experiments on a porphyritic basalt from the Reykjanes [*Adelinet et al.*, 2013], which is a microlitic alkali basalt with porosity of 11.2%.

Based on systematic microstructural observations on our failed samples and a synthesis of our data with other published mechanical data, we assess to what extent damage evolution associated with brittle fracture and compactive cataclastic flow in basalt can be analyzed with some of the existing micromechanical models, based on pore-emanated microcracking [*Sammis and Ashby*, 1986], sliding wing cracks [*Horii and Nemat-Nasser*, 1986; *Ashby and Sammis*, 1990], and pore collapse [*Curran and Carroll*, 1979; *Zhu et al.*, 2010].

2. Experimental Procedure

2.1. Sample Material and Preparation

The material used in this study was a lava flow basalt from Mount Etna volcano, one of the planet's few continuously active volcanoes. Our six blocks of basalt, named in what follows EB_I to EB_VI, were acquired from the quarry at the same location described by *Heap et al.* [2009]. As one of eight major rock types categorized by *Tanguy et al.* [1997] (on the basis of about 3000 thin sections and more than 300 whole-rock analyses), it is a porphyritic alkali basalt considered to be the most representative basalt from the volcano.

In hand specimen, one can observe many dark grey, angular phenocrysts embedded in a matrix that is light grey in color. Previous optical microscopy studies [*Tanguy et al.*, 1997; *Stanchits et al.*, 2006; *Heap et al.*, 2009] have identified the matrix to be a fine-grained groundmass (~60%) that includes crystals of primarily feldspar and smaller fractions of pyroxene and olivine. The phenocrysts, with effective diameters on the order of 0.1–1.0 mm, are composed of plagioclase, olivine, and pyroxene, with no discernable preferential alignment. Some of our blocks seem to have higher percentage of phenocrysts, but even among samples cored from the same block, spatial distribution of the phenocrysts can be heterogeneous.

Uniaxial compression tests were conducted in Strasbourg on 20 samples from the six blocks. Hydrostatic and triaxial compression experiments were also performed at the Stony Brook laboratory on nominally dry and water-saturated samples cored from the four blocks EB_I, EB_II, EB_III, and EB_IV. The two laboratories followed similar sample preparation and experimental protocols. However, dimensions of the cylindrical specimens were different. In Stony Brook the specimens had initial diameters of 18.4 mm and lengths of 38.2 mm, whereas those in Strasbourg had diameters of 20 mm and length of 40 mm. The samples were first dried in vacuum at 80°C for several days and then saturated with distilled water.

Porosity was measured using the water saturation technique on all the samples and with a helium pycnometer on a selection of samples. Porosity values determined by both techniques are in agreement within the measurement errors for an individual sample. Previous studies reported discrepancy in porosity values on basalt from Mount Etna, even on blocks from the same origin. To assess such variability, a total of 120 samples were prepared from the six blocks. Guided by the porosity measurements, 45 were selected for triaxial experiments and 20 for uniaxial experiments (Table 1).

The average values of the nominal connected porosity were found to be 4.7%, and 5% for EB_I and EB_III samples, respectively. Both blocks appeared homogeneous, and the porosity in both cases varied within ±0.2% around the average value. Significant variability in porosity was, however, observed in EB_II, EB_IV, and EB_V. Visual inspection of these blocks revealed a heterogeneous distribution of small ($<$1 mm) vesicles in some parts of the blocks. These variable vesicle concentrations resulted in sample porosities between 4.5

Table 1. Summary of Mechanical Data for the Samples Investigated in This Study

				Peak Stress		Compactive Yield Stress C*	
Sample	Block	Porosity(%)	Effective Pressure (MPa)	Differential Stress $Q=\sigma_1-\sigma_3$(MPa)	Effective Mean Stress $P=(\sigma_1+2\sigma_3)/3-P_p$(MPa)	Differential Stress $Q=\sigma_1-\sigma_3$(MPa)	Effective Mean Stress $P=(\sigma_1+2\sigma_3)/3-P_p$(MPa)
Ba_ud[a]	EB_I	4.7	0	139	46	-	-
Ba_1	EB_I	5.1	hydrostatic	-	-	-	-
Ba_4	EB_I	5.2	10	281	104	-	-
Ba_s1	EB_I	5.3	10	240	91	-	-
Ba_34	EB_I	4.8	10	221	84	-	-
Ba_23[a]	EB_I	4.7	10	327	120	-	-
Ba_16	EB_I	4.8	20	329	130	-	-
Ba_s2	EB_I	4.5	20	361	140	-	-
Ba_6	EB_I	4.9	30	399	164	-	-
Ba_19	EB_I	4.8	40	403	173	-	-
Ba_2	EB_I	5.1	50	500	217	-	-
Ba_38	EB_I	5.1	50	493	215	-	-
Ba_28	EB_I	4.8	50	561	238	-	-
Ba_62	EB_I	5.0	70	563	258	-	-
Ba_8	EB_I	4.9	80	560	267	-	-
Ba_36	EB_I	4.8	80	574	273	-	-
Ba_24[a]	EB_I	4.8	80	655	299	-	-
Ba_5	EB_I	4.2	100	658	320	-	-
Ba_12	EB_I	4.7	150	753	402	-	-
Ba_56[a]	EB_II	6.2	0	190	63	-	-
Ba_59[a]	EB_II	4.8	0	215	72	-	-
Ba_53	EB_II	8.1	50	365	170	-	-
Ba_52	EB_II	8.1	80	349	197	-	-
Ba_55	EB_II	7.9	150	-	-	411	287
EP_5[a]	EB_III	4.7	0	106	35	-	-
Ba_P4	EB_III	4.7	hydrostatic	-	-	-	-
Ba_P10	EB_III	5.1	10	224	85	-	-
Ba_P2	EB_III	4.8	50	434	195	-	-
Ba_P1	EB_III	5.0	80	543	261	-	-
Ba_P6	EB_III	4.8	100	640	313	-	-
Ba_P8	EB_III	4.9	150	798	417	-	-
EPo_11[a]	EB_IV	7.2	0	161	54	-	-
Ba_PO12	EB_IV	7.8	200	-	-	366	323
EBII_5[a]	EB_V	8.4	0	82	27	-	-
EBII_6[a]	EB_V	5.1	0	226	75	-	-
EBII_19[a]	EB_V	6.4	0	187	62	-	-
BB_1[a]	EB_VI	11.6	0	53	18	-	-
BB_2[a]	EB_VI	14.2	0	42	14	-	-
BB_3[a]	EB_VI	15.0	0	42	14	-	-
BB_4[a]	EB_VI	12.0	0	46	15	-	-
BB_7[a]	EB_VI	13.4	0	46	15	-	-
BB_8[a]	EB_VI	12.2	0	51	17	-	-
BB_9[a]	EB_VI	11.5	0	65	22	-	-
Rey_1[a]	Reykjanes	11.5	0	86	29	-	-
Rey_13	Reykjanes	11.4	0	72	24	-	-
Rey_2	Reykjanes	11.6	140	-	-	202	208
Rey_7	Reykjanes	11.3	200	-	-	143	248
Azo_1[a]	Azores	18.6	0	37	12	-	-

[a]Dry data.

and 8%. Triaxial experiments were performed only on samples from blocks EB_II and EB_IV with porosities at the high end (~8%). It is likely that mechanical behavior of samples with lower porosities in these two blocks would be similar to the EB_I and EB_III samples. Some variability was also observed in block EB_VI. The vesicles were significantly larger than in the other blocks (see Figure 5), reaching a size of 5 mm and sometimes more. With this significantly different and heterogeneous structure, our samples of EB_VI had porosities between 7.3 and 16%.

We observed a higher concentration of large phenocrysts in samples EB_III and EB_IV than in the other blocks. The matrix density (inferred from the bulk density and the porosity) was found to be 2.97 Mg/m^3 in these blocks and 2.86 Mg/m^3 in the other blocks with less phenocrysts. These values were confirmed by pycnometer measurements performed on powered samples from EB_I and EB_III, and these additional measurements suggested that most of the porosity is connected in the studied basalts. The observed difference in density is consistent with visual observation on the sample surface and also on thin sections which suggested between 15 and 25% more clinopyroxene phenocrysts in blocks EB_III and EB_IV.

We measured *P* wave velocity on a selection of samples and found an average of 3.38 ± 0.02 km/s and 3.35 ± 0.02 km/s for EB_I and EB_III, respectively. In EB_V with variable vesicle concentrations, V_p showed larger variations, in the interval 2.9–3.5 km/s, with no obvious relation to the porosity of the samples.

Permeability of samples from blocks EB_I, EB_III, and EB_VI was measured to be in the range 4×10^{-17} to 9×10^{-16} m^2 under ambient pressure and temperature (James Farquharson, personal communication), in basic agreement with previous measurements on Etna basalt by *Fortin et al.* [2010]. The higher end-members for permeability were obtained for the most porous samples of EB_VI.

For hydrostatic and triaxial compression experiments, each sample was jacketed with copper foil with a thickness of 0.05 mm and placed between two steel end-plugs, one of which had a piezoelectric transducer (PZT-7, 5.0 mm diameter, 1 MHz longitudinal resonant frequency) on its flat surface, and the other one had a concentric hole for fluid access to the pore pressure system. The copper jacket was used to avoid the development of unloading cracks (see *Zhang et al*. [1990] for details). Heat-shrink polyolefine tubing was then used to separate the sample from confining pressure medium (kerosene). For a nominally dry test, electric resistance strain gages (TML type PFL-10-11) were attached to the copper jacket in orthogonal directions to measure the axial and transverse strains. To circumvent the breakage of strain gages, we first filled larger surface pores with an epoxy (BLH SR-4 EPY-150). The sample was then jacketed with the copper foil. A hydrostatic pressure of 5 MPa was applied to "season" the copper jacket, and the strain gages were then glued on the jacketed sample. More details on the experimental procedure could be found in *Zhang et al*. [1990] and *Baud et al.* [2000].

2.2. Mechanical Deformation

The jacketed samples were deformed in conventional triaxial configuration at room temperature. Samples saturated with deionized water were deformed with the pore pressure maintained at 10 MPa under fully drained conditions. Two hydrostatic experiments were performed on samples of EB_I and EB_III up to effective pressures (difference between confining pressure and pore pressure) of 450 and 390 MPa, respectively. In these experiments, the confining pressure was increased by small steps of 5 to 20 MPa. At each step, we waited for full equilibrium (constant confining and pore pressures) before increasing the confining pressure. This guaranteed fully drained conditions for these hydrostatic experiments performed up to high effective pressures. For the triaxial experiments, the effective pressure ranged from 10 MPa to 200 MPa. To compare the mechanical behaviors between wet and dry samples, triaxial experiments under nominally dry conditions were also conducted. The confining pressure was monitored by a strain gage pressure transducer to accuracy of 0.1 MPa, and during triaxial loading it was held constant to within 1%. The axial load was measured with an external load cell with an accuracy of 1 kN. The axial displacement was servo-controlled at a fixed rate (corresponding to a nominal strain rate of 1.0×10^{-5} s^{-1}).

For saturated experiments, adjustment of a pressure generator kept the pore pressure constant, and the pore volume change was recorded by monitoring the piston displacement of the pressure generator with a displacement transducer (DCDT). The porosity change was calculated from the ratio of the pore volume change to the initial bulk volume of the sample. The axial displacement was measured outside the pressure vessel with a DCDT mounted between the moving piston and the fixed upper platen. For nominally dry experiments, the volumetric strain was calculated using the relation $\varepsilon_V = \varepsilon_{||} + 2\varepsilon_{\perp}$, where $\varepsilon_{||}$ and $\varepsilon_{\perp}$ are the strains measured in the axial and transverse directions, respectively.

The load, displacement, and strain gage signals were acquired by a 16-bit analog to digital converter at a sampling rate of 1 s^{-1} with resolutions of 0.3 MPa, 1 μm, and 10^{-5}, respectively. Uncertainty in strain was estimated to be 2×10^{-4} (when calculated from the DCDT signal) and 10^{-5} (when measured directly by the strain gages). Acoustic emission activity was monitored by the piezoelectric transducer attached to the sample.

2.3. Microstructural Analysis

Microstructure of intact and 15 triaxially deformed samples of EB_I, EB_II, and EB_III, compressed to different stages of deformation and then carefully unloaded, was studied using an optical microscope and scanning electron microscopes (SEM) on polished thin sections. Optical microscopy was performed using a Nikon optical polarizing microscope. For SEM observations, the gold-coated thin sections were studied at Stony Brook using a LEO 1550 microscope with a voltage up to 10 KV. Additional observations on deformed samples were performed at INGV Rome using a JEOL JSM-6500 F thermal field emission SEM. All SEM micrographs presented here were acquired in the backscattered electron mode.

3. Mechanical Data

Table 1 summarizes the deformation history of all basalt samples in this study. The convention is adopted that compressive stresses and compactive strains (i.e., shortening and porosity decrease) are positive. The maximum and minimum principal stresses will be denoted by σ_1 and σ_3, respectively.

3.1. Stress, Strain, and Failure Mode

Overall, the mechanical responses of EB_I and EB_III samples at effective pressures ranging from 0 MPa to 150 MPa were qualitatively similar (Figures 1a and 1d). The differential stress of a sample first attained a peak, beyond which strain softening was observed and the differential stress dropped to a residual level. Except for two samples deformed at the highest effective pressure of 150 MPa, instability with dynamic stress drop was observed in the postfailure stage of each sample. The failure mode is typical of the brittle faulting regime, with the development of a macroscopic fracture oriented at ~30° with respect to the σ_1 direction. The peak stress shows a positive correlation with the effective pressure and mean stress $(\sigma_1 + 2\sigma_3)/3$ (Table 1). The development of stress-induced damage was accompanied by a progressive increase in acoustic emission (AE) activity, as shown on Figure 1b for a EB_I sample deformed at an effective pressure of 150 MPa.

In comparison to EB_I and EB_III the mechanical responses of EB_II samples deformed at effective pressures ranging from 0 MPa to 150 MPa were quite different (Figure 1c). At effective pressures up to 50 MPa, the behavior of a sample was qualitatively similar to those of EB_I and EB_III samples, with the differential stress attaining a peak, beyond which there was a relatively small stress drop and the development of a shear band oriented at an angle of ~30° with respect to σ_1. Instability was not observed in the postfailure stage. The peak stress was significantly smaller than that of EB_I and EB_III at the same effective pressure. At the higher effective pressure of 80 MPa, shear localization was inhibited and the sample appeared to be on the transition from brittle faulting to cataclastic flow. A plateau (Figure 1c) on the stress-strain curve was observed with no obvious stress drop. At effective pressures larger than 80 MPa, the EB_II samples typically showed continuous strain hardening and failed by distributed cataclastic flow (Figure 1c).

To illustrate the development of inelastic volume change, we show in Figure 2 our data for the effective mean stress (difference between the mean stress and pore pressure) as a function of porosity reduction. For reference, hydrostats for EB_I and EB_III samples were also shown as the dashed curves. The hydrostatic compression experiments were conducted on EB_I (Figure 2a) and EB_III (Figure 2c) samples with effective pressures up to 450 and 390 MPa, respectively. An inflection point that corresponds to the onset of pore collapse was not observed during either experiment, which implies that the threshold pressures for pore collapse are higher than the maximum pressures attained. The hydrostatic responses were nonlinear up to a pressure of ~250 and 150 MPa for the EB_I and EB_III samples, respectively. Beyond these critical pressures for elastic crack closure, the hydrostats became linear and extrapolation of the linear trends allows one to infer the preexisting crack porosities [*Walsh*, 1965]. As illustrated in the figures, the crack porosities of the EB_I and EB_III samples so inferred are 0.85% and 0.92%, respectively.

The triaxial compression curves for EB_I and EB_III samples were qualitatively similar. At a given effective pressure, the triaxial curve would basically coincide with the hydrostat up to a critical stress state *C′* (as marked in Figure 2a for the data at effective pressure of 20 MPa), beyond which there was a decelerated reduction of porosity, implying an inelastic dilation of the pore space. Thus, *C′* corresponds to the onset of dilatancy, the point at which the volume of the triaxially compressed sample became greater than that of the hydrostatically compressed counterpart at the same mean stress. The differential stress level at *C′* for EB_I and EB_III samples showed positive pressure dependence.

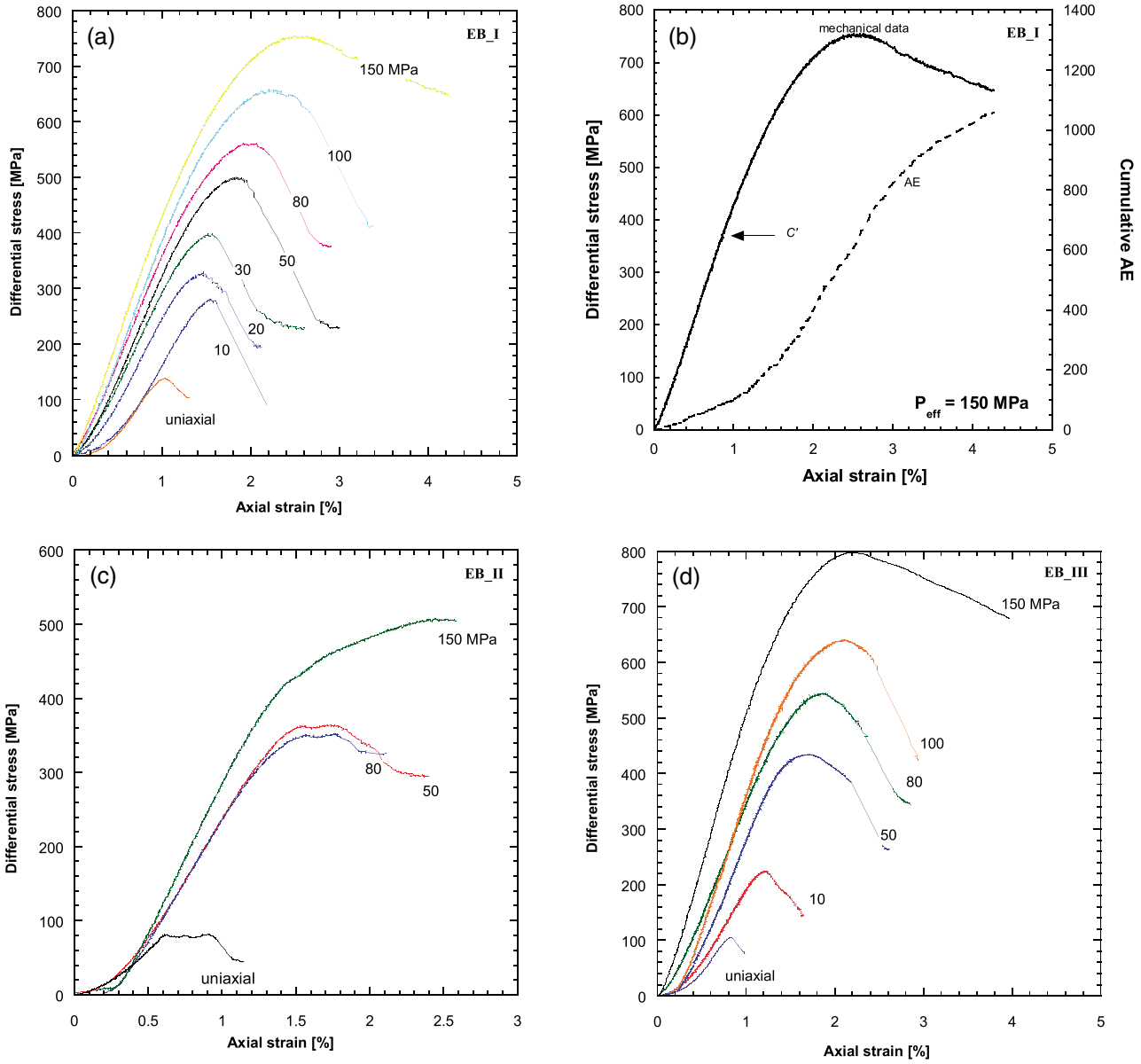

Figure 1. Mechanical data for wet experiments on (a and b) EB_I block, (c) EB_II block, and (d) EB_III block of Etna basalt. Differential stress is plotted versus axial strain (Figures 1a–1c). Numbers next to each curve indicate the effective pressure maintained during the experiment. Samples deformed under uniaxial conditions were not saturated. Differential stress and cumulative number of acoustic emissions for a sample of EB_I block deformed at an effective pressure of 150 MPa (Figure 1b). The AE activity increased significantly at the onset of dilatancy *C'* marked on the graph by an arrow.

Given what is known regarding permeability and specific storage, as well as dimensions of our basalt samples, we can infer the characteristic time required to effectively drain any pore pressure excesses induced by the deformation and conclude from such analysis that the strain rate in our triaxial experiments was sufficiently slow to inhibit the development of an undrained condition. A more direct validation is by comparing the hydrostatic and triaxial data (Figure 2a). As noted earlier, our hydrostatic tests were conducted in a manner to ensure fully drained condition. The very nice coincidence between the hydrostat and the triaxial data prior to *C'* confirmed that indeed our triaxial experiments were performed under fully drained conditions. Dilatancy beyond *C'* is expected to enhance the permeability and drainage, rendering it ever more difficult to build up pore pressure excess in the sample.

Due to the limited number of samples from this block, we did not perform a hydrostatic compression experiment on a EB_II sample. Nevertheless, we managed to infer from the triaxial compression data (Figure 2b)

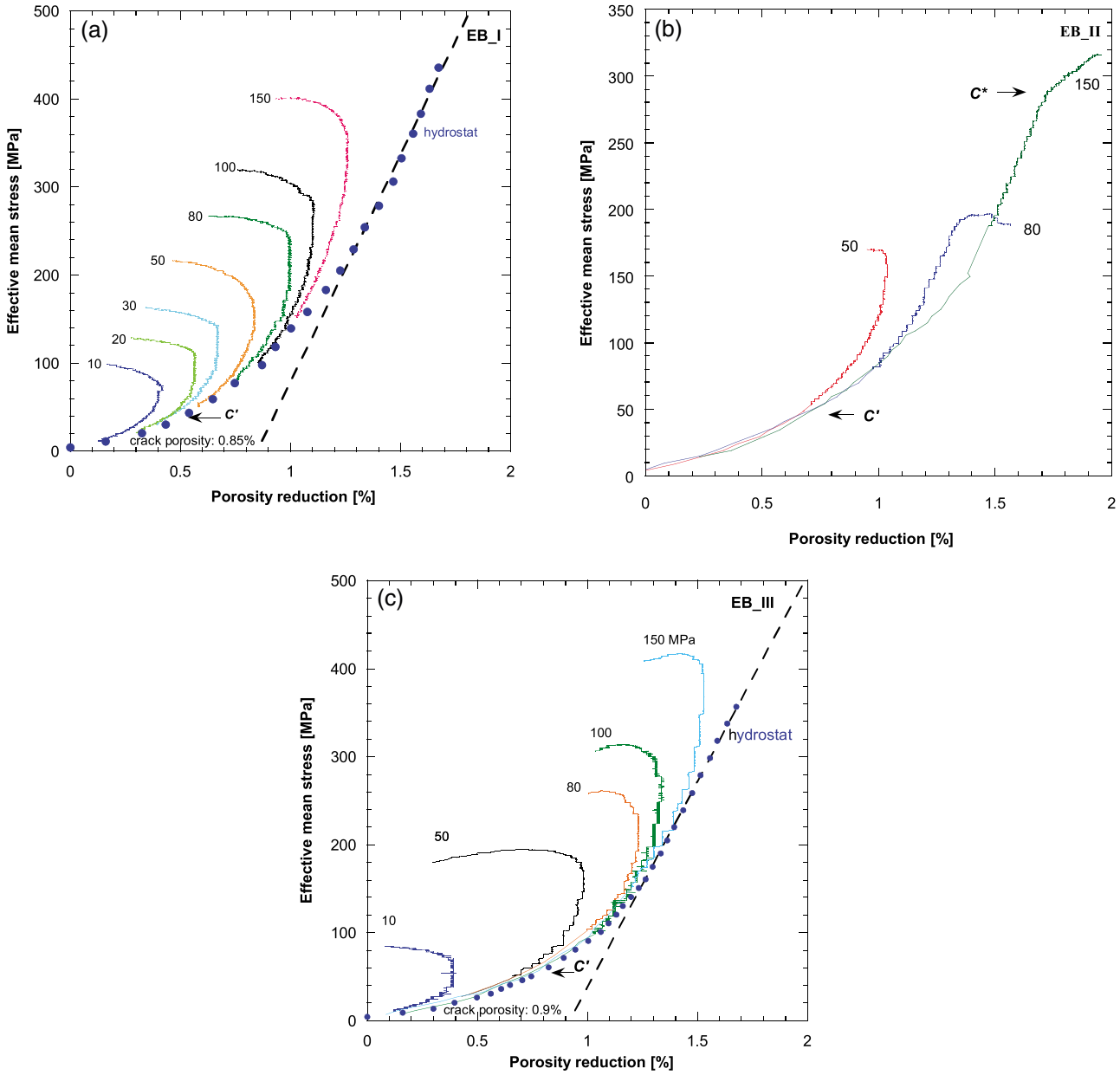

Figure 2. Effective mean stress is plotted as a function of porosity reduction on (a) EB_I block, (b) EB_II block, and (c) EB_III block of Etna basalt. Numbers next to each curve indicate the effective pressures maintained during the experiments. For reference, hydrostatic data are shown as the dashed curve for EB_I and EB_III blocks. The onset of dilatancy *C'* in experiment at effective pressure of 50 MPa is marked by arrows. The onset of shear-enhanced compaction *C** in the experiment at effective pressure of 150 MPa is marked by an arrow in EB_II block. For EB_I and EB_III, the linear part of the hydrostats is fitted by linear regression and the microcrack porosity is indicated.

that whereas dilatancy was associated with the sample deformed at effective pressure of 50 MPa, a fundamentally difference behavior was observed in the two samples deformed at elevated pressures of 80 MPa and 150 MPa. In the latter case, beyond a critical stress there was an accelerated decrease in porosity which implies that the deviatoric stress field provided significant inelastic contribution to the compactive strain. This critical stress state *C** corresponds to the onset of shear-enhanced compaction [*Wong et al.*, 1997].

3.2. Comparison of Nominally Dry and Saturated Samples

To investigate the effect of water, we compared the mechanical behaviors of the saturated samples with nominally dry basalt samples from the EB_I block (Figure 3). The experiments were conducted at

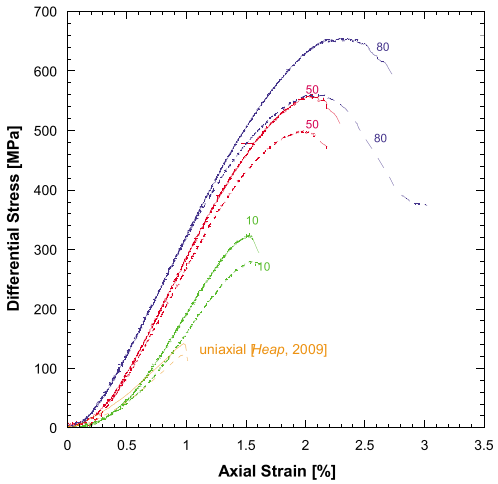

Figure 3. Comparison of mechanical data between nominally dry and water-saturated EB_I samples. Differential stress is plotted as a function of axial strain. Numbers next to each curve indicate the effective pressure (confining pressure) imposed during the experiment. Stress-strain curves for dry and wet conditions are represented by solid and dashed line, respectively.

effective pressures of 10 MPa, 50 MPa, and 80 MPa. For comparison we also include uniaxial compression data of *Heap* [2009]. While the mechanical response and failure mode for dry and wet samples were qualitatively similar, a dry sample typically attained a higher peak stress than a saturated one.

4. Microstructural Observations

Our microscopy observations on an undeformed EB_I sample basically confirm earlier reports on texture and microstructure of the Etna basalt [*Tanguy et al.*, 1997; *Stanchits et al.*, 2006; *Heap et al.*, 2009]. The solid fraction of the sample comprises a number of relatively large phenocrysts embedded in a microcrystalline matrix. The phenocrysts have effective diameters (considering the equivalent disk of same area) up to ~400 μm (Figure 4a). Macropores (equant voids) exhibit effective diameters up to 200 μm. We consider here as in previous studies (see for example *Zhu et al.* [2010]) a threshold between macropore and micropore for a radius of 33 μm.

Under the SEM (Figures 4b and 4c), a multiplicity of microcracks with lengths on the order of 10 to 100 μm can be observed. They are present not only in the matrix but also as intragranular cracks inside the phenocrysts. *Vinciguerra et al.* [2005] suggested that many of these were induced by thermal shock due to the fast rate of

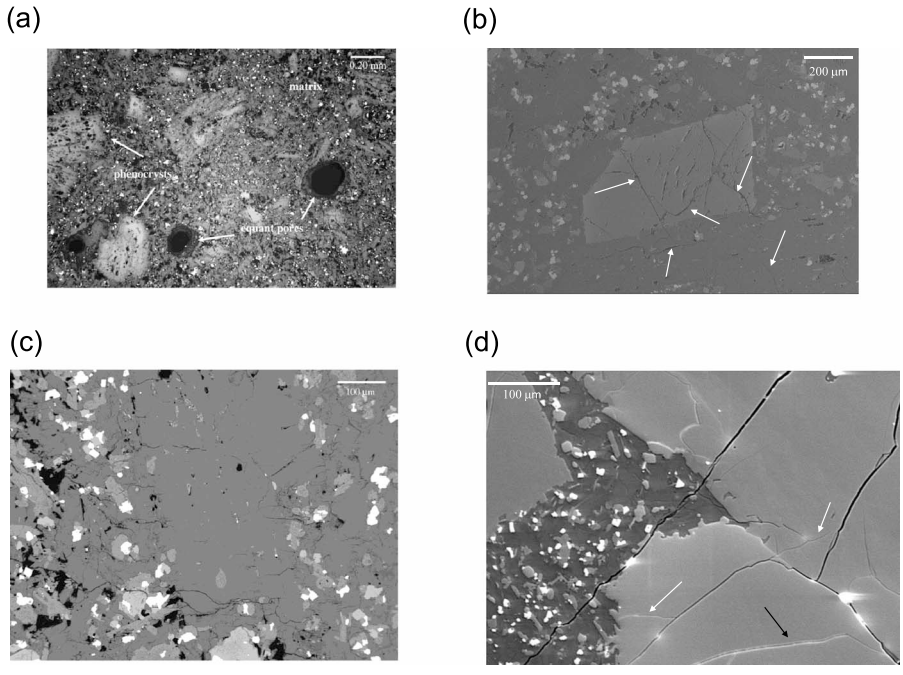

Figure 4. (a) Optical micrograph of intact EB_I basalt sample. Phenocrysts and equant pores are marked in the image. Macropores with radius around 100 μm were observed as shown by the dark areas. (b) Backscatter SEM image of intact EB_I sample. A phenocryst grain with sharp edges was embedded in the matrix. Preexisting microcracks within the phenocryst and in the matrix are marked by solid and dashed arrows, respectively. (c) Backscatter SEM image of intact EB_I sample. Numerous healed or sealed microcracks with length around 50 μm were observed in the matrix. (d) Backscatter SEM image of intact EB_I sample. The relatively thin cracks indicated by arrows have been sealed. One of the wider cracks indicated by a black arrow has been partially filled with bridges.

Figure 5. Photograph of the sample BB_2 from block EB_VI deformed uniaxially to failure. Pore-emanated cracking is visible on the surface of the sample.

cooling in lava flows. Under higher magnifications, opposite sides of these cracks seem smooth and mated, suggestive of an origin related to thermal cracking. Most of the relatively thin cracks have been sealed (Figure 4d). There are also cracks with wider apertures that have been partially filled by "bridges." Nevertheless, the microcracks that remain open do contribute a significant crack porosity of 0.85%, as inferred from our hydrostatic compression data for EB_I (Figure 2a). Some micropores (with diameters one the order of 1 μm or less) can also be observed; they are not as abundant as those in a limestone [*Zhu et al*., 2010] or a tuff [*Zhu et al*., 2011].

4.1. Brittle Faulting

Under uniaxial compression, the stress concentration at macropores induces microcracks to emanate and propagate subparallel to the σ_1 direction. The pore-emanated crack can propagate to a distance comparable to the pore diameter. This mode of damage and failure is illustrated in a EB_VI sample of 14.2% porosity with millimeter-sized macropores (Figure 5). A pore-emanated crack propagated almost all the way toward the bottom of the sample. Another one propagated upward, intersected, and was arrested by a macropore. Ultimately, a number of pore-emanated cracks coalesced to develop a shear band that cut through the upper half of the sample.

Two EB_I samples were deformed to beyond the onset of dilatancy in the prefailure stage at effective pressures of 10 MPa (Figure 6a) and 50 MPa (Figure 6b), respectively. In both samples stress-induced cracking has developed primarily by the reopening of healed and sealed cracks, preferentially aligned with the σ_1 direction. A few relatively short cracks were observed to have emanated from macropores (Figure 6a). A relatively long crack seems to have developed by linking up several preexisting cracks and wing crack propagation (Figure 6b). Our observations of extensive reopening of healed and sealed cracking induced by stress in Etna basalt are qualitatively similar to those in San Marcos gabbro reported by *Wong and Biegel* [1985].

Figures 7a and 7b illustrate the development of shear bands at effective pressure of 80 MPa in EB_I and EB_III samples, respectively. These samples underwent unstable stress drops that were probably associated with slip along a primary band, but it can be seen that a number of incipient shear bands had also developed. In the vicinity of the primary shear band in the EB_III sample, coalescence of stress-induced cracks (Figure 8a) and pore-emanated cracks (Figure 8b) can be observed. Although intragranular cracking have developed within the phenocrysts, there seems to be a tendency for cracking to avoid cutting through the phenocrysts, as indicated by the propagation of such cracks along the phenocryst boundaries in the EB_I (Figure 8c) and EB_III (Figure 8b) samples.

4.2. Inelastic Compaction

The micromechanics of shear-enhanced compaction was investigated in two EB_II samples deformed at effective pressures of 80 MPa and 150 MPa to beyond the yield stress C^*. In the former sample, we observed a complex interplay of dilative and compactive damages: transgranular cracking that seems to avoid cutting through phenocryst (Figure 9a), and pore-emanated cracks (Figure 9b), as well as collapse of macropore (Figure 9c). In the sample deformed at an effective pressure of 150 MPa, we observed two macropores at different stages of damage evolution: a macropore surrounded by a halo of cataclastic damage (Figure 9d), and a macropore that has ultimately collapsed (Figure 9e). The damage evolution is akin to that observed in porous limestone [*Zhu et al*., 2010] and tuff [*Zhu et al*., 2011].

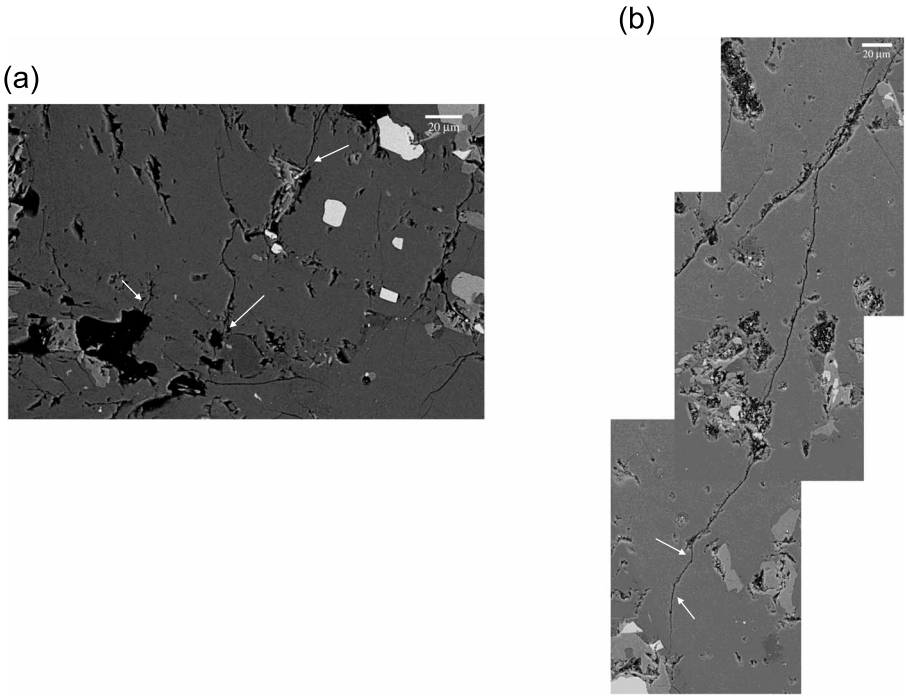

Figure 6. Backscatter SEM images of EB_I basalt samples failed by brittle faulting. Direction of σ_1 is vertical. (a) A sample was loaded beyond the onset of dilatancy *C'* under effective pressure of 10 MPa. Short cracks were observed to have emanated from macropores as indicated by white arrows (b) A sample was compressed beyond *C'* under an effective pressure of 50 MPa. Stress-induced cracks had propagated over a long distance (on the order of 100 μm) in a direction subparallel to σ_1. Wing cracks were observed to propagate subparallel to σ_1 as indicated by white arrows.

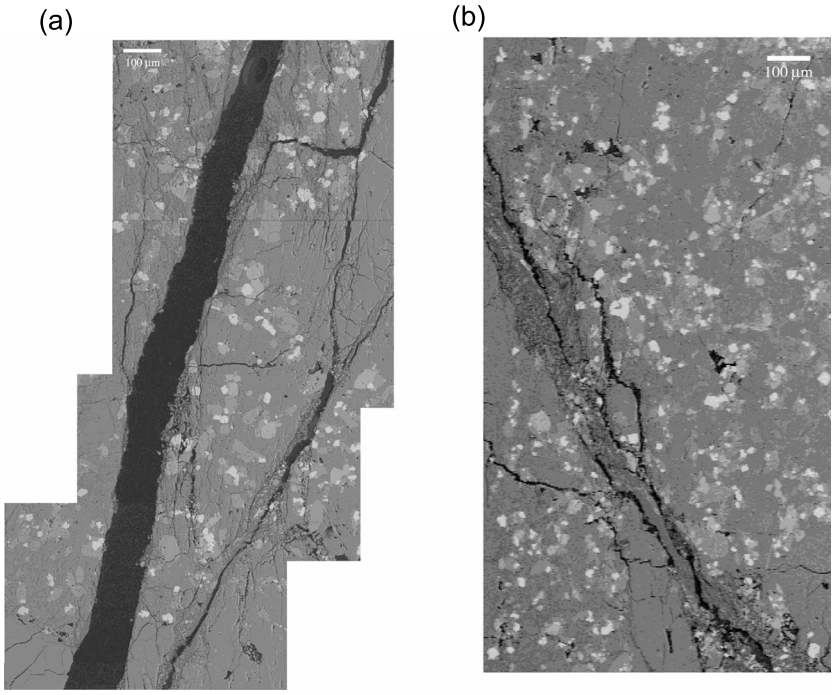

Figure 7. Shear localizations in (a) EB_I and (b) EB_III samples are illustrated in the left and right images, respectively. Both samples were loaded after the peak (up to 3% axial strain) under the same effective pressure of 80 MPa. Intense microcracking and comminution were observed in the vicinity of the shear bands. There were more phenocrysts embedded in the matrix in EB_III sample than EB_I sample. The shear band in EB_I was much wider than that in EB_III sample. Direction of σ_1 is vertical.

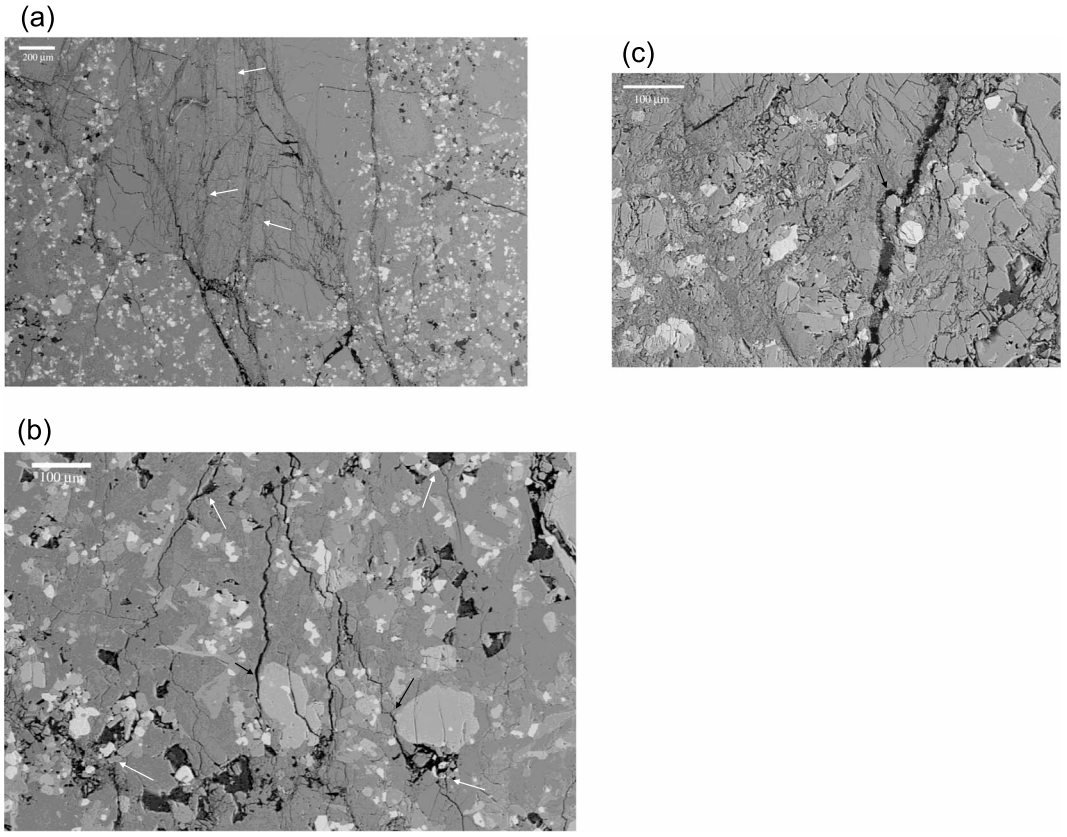

Figure 8. Backscatter SEM images of Etna basalt samples failed by brittle faulting. Direction of σ_1 is vertical. Images were taken in the vicinity of the shear bands shown in Figure 7 in samples of (a and b) EB_III and (c) EB_I loaded beyond the peak stress under an effective pressure of 80 MPa. Numerous stress-induced microcracks were observed to propagate and coalesce in the matrix in a direction subparallel to σ_1.Coalescence of stress-induced cracks (Figure 8a) and pore-emanated cracks (Figure 8b) are visible in the sample of EB_III and indicated by white arrows. Microcracks propagated along the phenocryst boundaries in the EB_I (Figure 8c) and EB_III (Figure 8b) samples, as indicated by black arrows.

5. Discussion

The development of dilatancy and micromechanics of brittle faulting in compact crystalline rocks and porous siliciclastic rocks has been extensively investigated [*Paterson and Wong*, 2005]. Preexisting microcracks and pores can readily nucleate stress-induced damage, and shear localization develops by coalescence of the stress-induced cracks. Our earlier study of tuff [*Zhu et al*., 2011] and the current investigation of basalt have shown that the brittle faulting processes in these volcanic rocks involve similar processes.

The pore spaces of basalt and tuff are similar to that of porous limestone in that they contain numerous macropores. Recent studies of limestones [*Zhu et al*., 2010; *Vajdova et al*., 2010, 2012] and tuffs [*Zhu et al*., 2011] have shown that these macropores play an important role in the nucleation of stress-induced microcracks and their coalescence ultimately leads to brittle faulting. Our observations here indicate that indeed this mechanism of pore-emanated cracking can be important for uniaxial compressive failure, especially in the more porous basalt samples. However, in the less porous samples (EB_I and EB_III) our observations also indicate that this mechanism is not as important under confinement, and brittle failure seems to derive primarily from wing crack growth and coalescence, which can readily be induced by stress because of the abundance of preexisting damage in the form of open and healed cracks.

As for inelastic compaction and cataclastic flow, our observations indicate that the phenomenology in a relatively porous basalt (EB_II) is qualitatively similar to that in a sandstone [*Wong et al*., 1997], limestone [*Vajdova et al*., 2004], and tuff [*Zhu et al*., 2011]. Notwithstanding these similarities, recent studies also underscore that the micromechanics in limestone and tuff is very different from that in a sandstone, which involves primarily grain crushing initiated by the stress concentrations at grain contacts [*Menéndez et al*., 1996]. Our study of

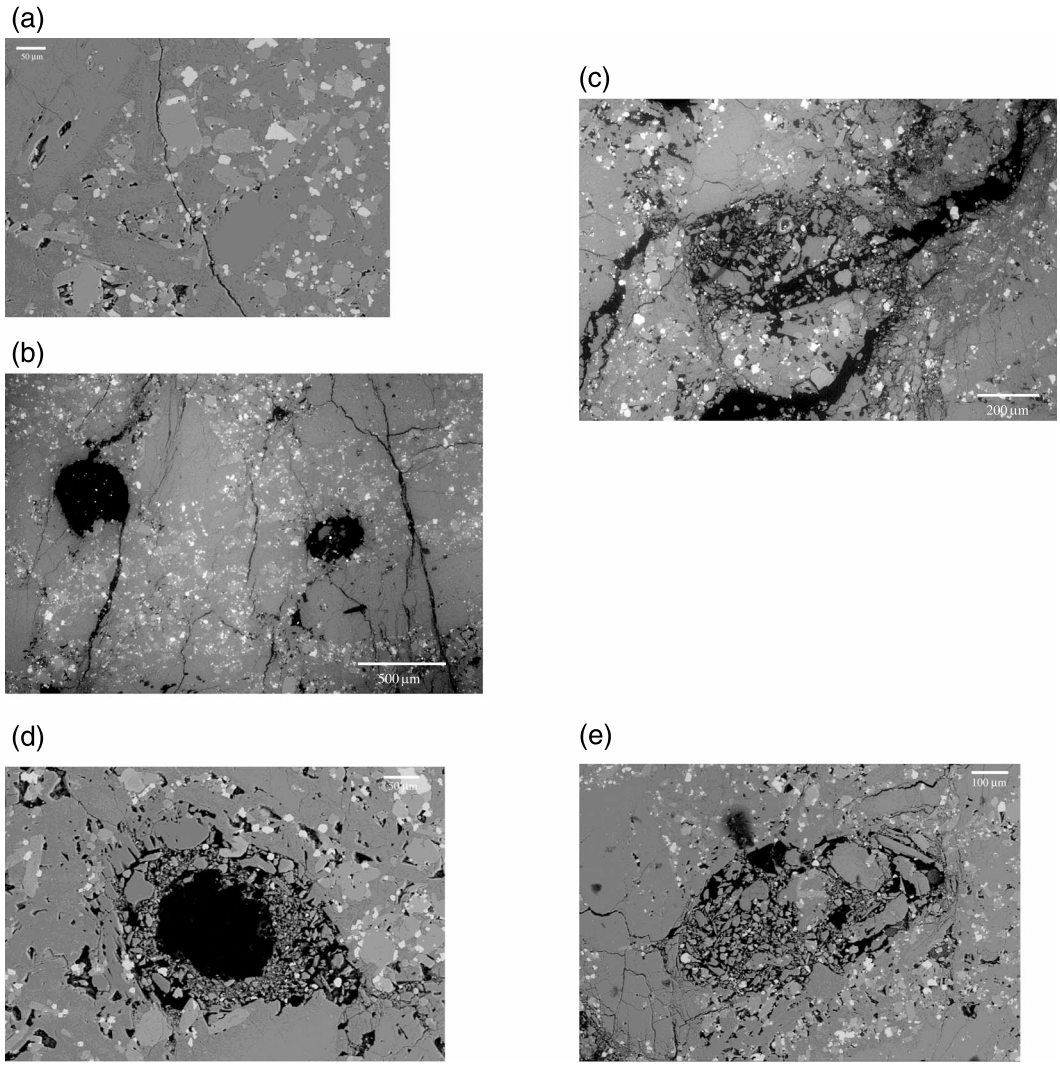

Figure 9. Backscatter SEM images of EB_II basalt samples failed by inelastic compaction. Direction of σ_1 is vertical. (a) A sample was loaded beyond the onset of shear-enhanced compaction C^* under an effective pressure of 80 MPa. A stress-induced crack was observed to propagate subparallel to σ_1 and seems to avoid cutting through the phenocryst. (b) Pore-emanated microcracking and (c) collapse of a macropore in the same sample. A sample was loaded beyond C^* under an effective pressure of 150 MPa: (d) Macropore with a radius on the order of 100 μm surrounded by a halo of cataclastic damage. The damage zone had extended a distance of ~100 μm. (e) Collapsed macropore in the same sample. Crushed grains had fallen into the interior of the macropore.

basalt has shown that in some respects, its behavior is similar to that in porous limestones and tuffs [*Vajdova et al*., 2010; *Zhu et al*., 2011], which typically involves pore collapse that initiates from stress concentrations at the periphery of the macropores. Nevertheless, it should also be noted that there is a subtle difference. In limestone the micromechanical process has been captured by a "dual-porosity" model, made up of macropores embedded in a matrix comprising numerous micropores [*Zhu et al*., 2010]. However, in Etna basalt there are fewer micropores, and instead, the numerous preexisting microcracks seem to play a similar role in conjunction with the macropores to constitute a dual-porosity medium.

5.1. Uniaxial Compressive Strength

Our data for six blocks of Etna basalt indicate an overall trend for the uniaxial compressive strength (UCS) to decrease with increasing porosity (Figure 10). There is variation of mineralogy among the six blocks. Likewise, the ratio of phenocryst to microcrystalline groundmass varies. As mentioned in section 2.1, a larger proportion of big phenocryst in blocks EB_III and EB_IV resulted in a matrix density about 10% larger in these blocks

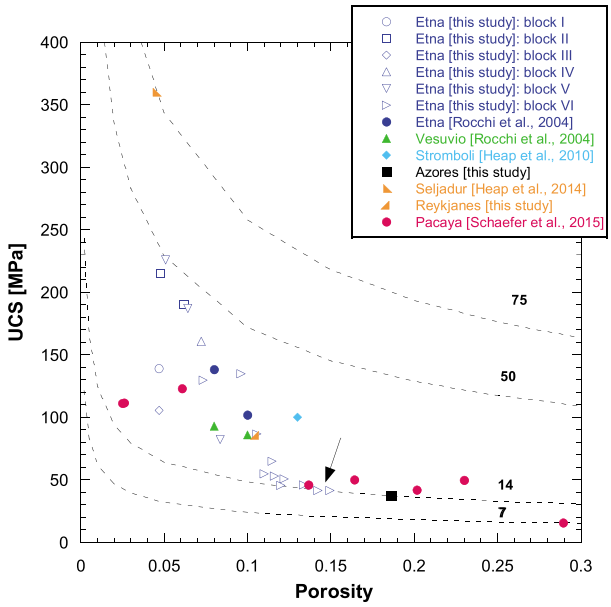

Figure 10. Comparison of theoretical predictions with laboratory data on UCS of basalt. UCS is presented as a function of porosity. Theoretical curves of UCS (equation (1)) are also presented. The arrow on the graph shows the sample BB_2 (Figure 5). Measurement errors are less than the symbol sizes.

than in the others. Nevertheless, the influence of composition and phenocryst content on the UCS seems secondary in comparison to the dominant effect of porosity.

We also acquired UCS data on two other porphyritic basalts: the Azores and Reykjanes basalt samples are considered to be identical to the blocks of *Loaiza et al.* [2012] and *Adelinet et al.* [2013], respectively. In Figure 10 we have included other published data on basalt. The Vesuvian sample investigated by *Rocchi et al.* [2004] was a porphyritic basalt made up of 20% euhedral phenocrysts and 80% glassy/cryptocrystalline groundmass, with numerous macropores up to 1 mm in diameter. The Stromboli basalt investigated by *Heap et al.* [2010] was made up of 40% phenocrysts and 60% microcrystalline groundmass, with significant crack porosity attributed to rapid thermal cooling. The samples from Pacaya, Guatemala, investigated by *Schaefer et al.* [2015] were porphyritic basalts made up of 45% phenocrysts embedded in a microlitic groundmass. The basalt from Seljadur, Iceland, investigated by *Heap et al.* [2010] had a microlitic groundmass, with few pre-existing microcrack porosity. Its porosity was confirmed to be 4.5% by *Heap et al.* [2014], who corrected underestimates that had been reported in the literature.

The data compiled in Figure 10 are all for nominally dry samples. There is an overall trend for water-saturated samples to be appreciably weaker, a phenomenon possibly related to the weakening in the presence of water, which we will discuss in a latter section. Although the formation of these basalts involved a diversity of volcanic processes and thermal histories, their UCS data show a systematic correlation with the total porosity. In light of this apparent correlation and our observation of the failure mode in the more porous samples (Figure 5), we will first interpret this trend using the pore-emanated cracking model of *Sammis and Ashby* [1986], which would predict a one-to-one correspondence between UCS and porosity for rocks with similar pore sizes. The two-dimensional damage mechanics model considers an elastic medium pervaded by circular holes of uniform radius r. As the applied stress increases, a point is reached when the stress intensity factor of a small crack on the circular surface attains the critical value K_{IC}, at which point extensile cracks would initiate from the poles and propagate to a certain distance parallel to the σ_1 direction. As the stress-induced cracks propagate to longer distances with increasing stress, they interact with one another to induce an additional tensile stress intensity, ultimately leading to an instability with coalescence of the pore-emanated cracks at the peak stress level.

At a fixed lateral stress, *Sammis and Ashby*'s [1986] pore-emanated cracking model predicts that the peak differential stress scales with the parameter $K_{IC}/\sqrt{\pi r}$. For uniaxial compression, *Zhu et al.* [2010] obtained an analytic estimate of the UCS, σ_u, as a function of porosity Φ:

$$\sigma_u = \frac{1.325}{\Phi^{0.414}} \frac{K_{IC}}{\sqrt{\pi r}} \tag{1}$$

We compare in Figure 10 this analytic approximation with our compiled UCS data for dry basalt. For porosities above 15%, the model of *Sammis and Ashby* [1986] predicts that for the same rock composition the UCS is mostly controlled by the pore size. Most of the data for basalt from seven different volcanic regions with porosities ranging from 1.2% to 28.9% can be bracketed by equation (1) for $K_{IC}/\sqrt{\pi r} = 14$ and 50 MPa.

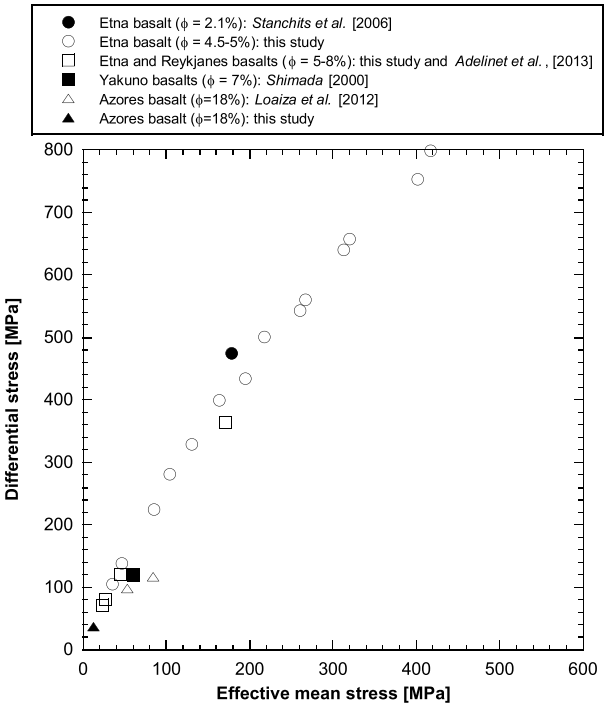

Figure 11. Peak stresses for samples of EB_I, EB_II, and EB_III that failed in the brittle manner are plotted in the stress space. For reference, peak stress data for Yakuno, Reykjanes (squares), and Azores (triangles) basalts are also shown. Dry and wet data are shown as solid and open symbols, respectively.

According to experimental measurements on common silicate minerals, the value of K_{IC} is ~0.3 MPa m$^{1/2}$ for feldspars and can be higher (but not by an order of magnitude) in other silicate minerals such as quartz and olivine. However, if the induced cracking develops along a healed or sealed crack, K_{IC} is expected to be lower, possibly by a factor of 2 or so [*Atkinson and Meredith*, 1987]. As elaborated in a latter section, its value is also expected to be lower in the presence of water. If we were to assume $K_{IC} = 0.3$ MPa m$^{1/2}$, then according to equation (1) the laboratory data for UCS of basalts are bracketed by average macropore size ranging from $r = 5$ μm to 585 μm. It should be emphasized that the *Sammis and Ashby* [1986] model assumes pores of uniform size, and the parameter r corresponds to the average size.

For the sample from block EB_VI shown in Figure 5, its preexisting pores may be as large as multiple grains, and given the transgranular nature of the observed pore-emanated cracks, it is more appropriate to use the K_{IC} value for the polycrystalline rock, which would imply a pore diameter of $2r$~1.1 cm, comparable to few very large pores visible on the sample surface. It should also be emphasized that the model prediction hinges on accurate porosity measurements. Reassessment of published data indicates that some of them may have underestimated the basalt porosity. A typical case is Seljadur basalt from Iceland, for which *Vinciguerra et al.* [2005] initially reported a porosity of about 1% and *Heap et al.* [2014] later estimated it to be 4.5% on the same block. While the reason for this type of discrepancy is unclear, if indeed the porosity of a basalt has been underestimated, then the inferred pore size in Figure 10 would represent an upper bound. It is likely that the discrepancy is more pronounced for a basalt with porosity of $<$10%.

5.2. Confined Compressive Strength

In a triaxially compressed basalt, our microstructural observations indicate that the micromechanics of brittle failure is dominated by wing crack growth related to the preexisting open and healed cracks, with pore-emanated cracking playing a secondary role. The mechanical data (Figure 11) also corroborate this suggestion. We compile the confined compressive strength data for four basalts with porosities ranging from 2.1 % to 18.0%. Compared to our EB_I and EB_III samples (with intermediate porosities of ~5%), the data of *Stanchits et al.* [2006] for a low-porosity Etna basalt and those for the more porous Yakuno [*Shimada*, 2000], Reykjanes [*Adelinet et al*., 2013], and Azores [*Loaiza et al*., 2012] basalts seem to be somewhat higher and lower, respectively. This suggests a slight trend for the brittle strength to decrease with increasing porosity, but this apparent dependence on porosity is much weaker than what would be predicted by the pore-emanated crack model [*Sammis and Ashby*, 1986].

A micromechanical model that has been used extensively to describe processes akin to our microstructural observations in triaxially compressed basalt samples is the sliding wing crack model [*Horii and Nemat-Nasser*, 1986; *Ashby and Sammis*, 1990; *Kemeny and Cook*, 1991]. The model considers sources of tensile stress concentration that are located at the tips of preexisting cracks. The applied far-field stresses induce a shear traction on the crack plane (of length $2c$), and if the resolved shear traction exceeds the frictional resistance along the closed crack, frictional slip occurs which also induces tensile stress concentrations at the two tips

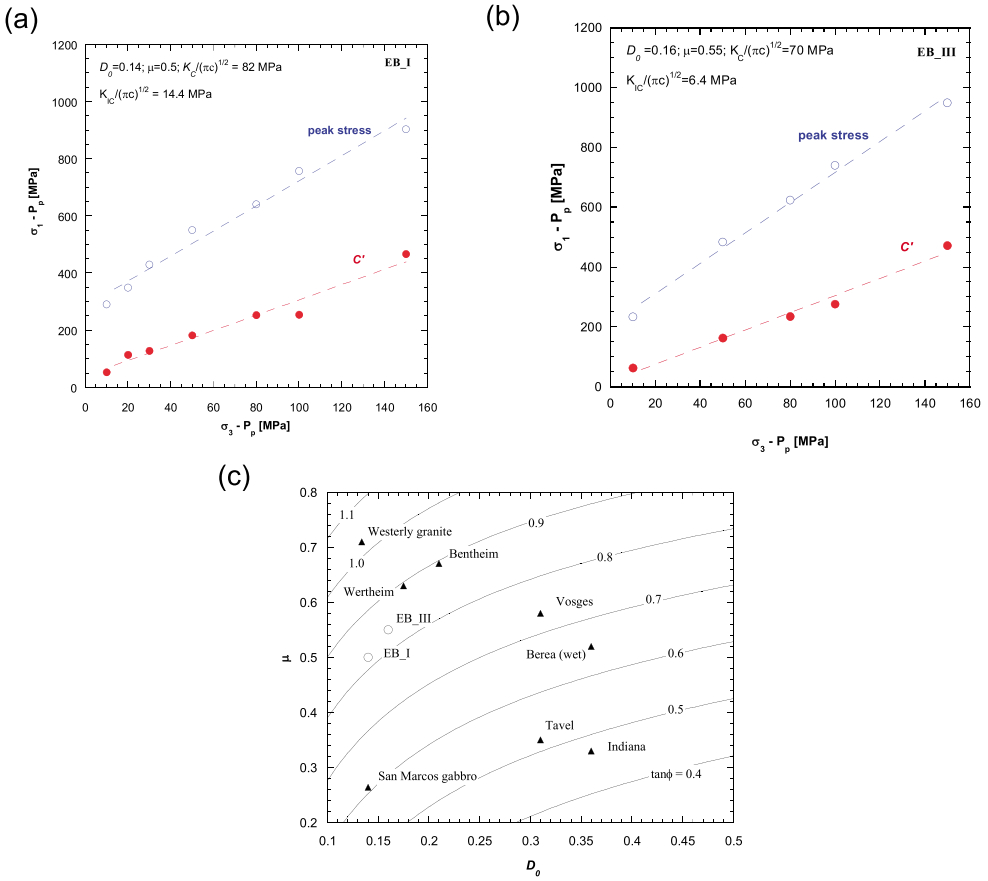

Figure 12. Comparison of the experimental data on brittle faulting (onset of dilatancy *C′* and the peak stress) for (a) EB_I and (b) EB_III basalt with predictions based on *Ashby and Sammis* [1990] wing crack model. The onset of dilatancy *C′* and peak stress are represented by solid and open circles, respectively. The linear fit is shown with parameter values as indicated. (c) The solid curves represent contours of equal coefficient of internal friction (tanφ) in the space of friction coefficient μ and initial damage D_0 according to the sliding wing crack model. EB_I and EB_III data are represented by open circles. For comparison, experimental data and inferred values of eight other rocks compiled by *Zhu et al.* [2010] are shown as solid triangles.

that may nucleate and propagate wing cracks parallel to the σ_1 direction. As wing cracks grow to longer distances, they interact and ultimately coalesce to result in an instability.

In the brittle faulting regime, inelastic deformation accompanied by dilatancy is typically observed prior to the attainment of the peak stress. If the onset of dilatancy *C′* is identified with the initiation of wing cracks and if the rock is assumed to contain randomly oriented cracks, then the sliding wing crack model predicts that the maximum and minimum principal stresses at *C′* would fall on a linear trend, with slope and intercept related to frictional coefficient μ, fracture toughness K_{IC}, and half-length *c* of the preexisting sliding crack. If the wing crack initiates from an intragranular location, it is appropriate to assume a K_{IC} value comparable to fracture mechanics measurements on the minerals that form the rock.

Mechanical data for many rocks indicate that principal stresses at the onset of dilatancy indeed follow an approximately linear trend, and one can accordingly infer from the slope and intercept the two micromechanical parameters μ and $K_{IC}/\sqrt{\pi c}$ [*Ashby and Sammis*, 1990; *Baud et al.*, 2000; *Vajdova et al.*, 2004; *Baud et al.*, 2014]. Following this approach, we fitted the *C′* data for saturated samples of EB_I (Figure 12a) and EB_III (Figure 12b) to straight lines and inferred by linear regression the two micromechanical parameters. The $K_{IC}/\sqrt{\pi c}$ values so inferred are sensitively dependent on the scatter and uncertainty in picking the *C′* data. It should be noted that both fitted lines have intercepts close to the origin. Assuming again $K_{IC} = 0.3$ MPa $m^{1/2}$ and noting that the preexisting cracks have lengths on the order of 10–100 μm (and therefore half-lengths $c = 5$–50 μm), we would expect the value of $K_{IC}/\sqrt{\pi c}$ to fall between 23.9 and 75.7 MPa,

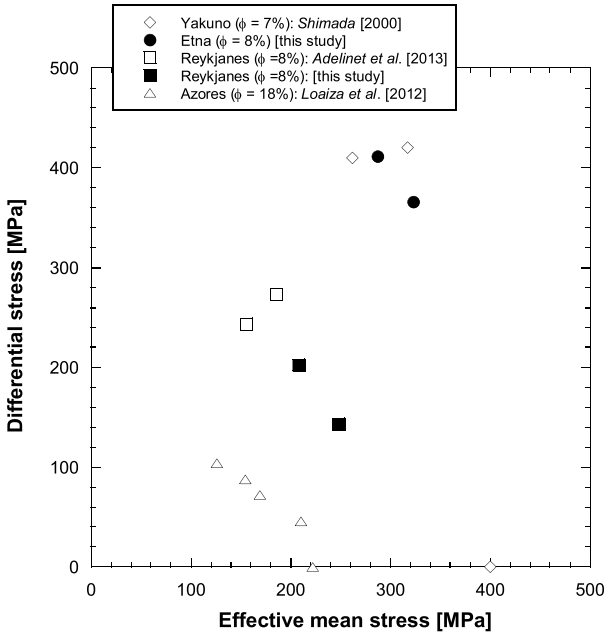

Figure 13. Critical stresses C^* for the onset of shear-enhanced compaction are plotted in the *stress* space for Etna, Yakuno [*Shimada*, 2000], Reykjanes [*Adelinet et al*., 2013], and Azores [*Loaiza et al*., 2012] basalts. There is an overall trend for the yield caps (C^*) to expand with decreasing porosity.

which is significantly larger than the inferred values of 14.4 MPa and 6.4 MPa (Figure 12). The discrepancy is likely due to K_{IC} values associated with reopening of healed and sealed cracks in the basalt that are much lower than mineral values for propagation of a newly introduced fracture.

At the peak stress, the sliding wing crack model predicts that the principal stresses would also fall on a linear trend, with slope and intercept related to the crack length, friction coefficient and fracture toughness, as well as an additional nondimensional parameter D_o that characterizes the "initial damage" (or "crack density") and is proportional to the number of preexisting cracks per unit area and the crack length square (in the two-dimensional model). Since instability at the peak stress is associated with coalescence of a multiplicity of stress-induced cracks, the operative micromechanical processes are expected to be complex, involving intragranular, intergranular, and transgranular cracking and possibly a hybrid of modes I, II, and III. In their analyses of brittle faulting data for a variety of rock types, *Baud et al.* [2014] concluded that it is likely that the critical stress intensity factor at this instability stage would have a value significantly higher than the K_{IC} value for mode-I cracking in the minerals. Accordingly, they proposed the use of a different notation K_C for this fracture toughness applicable at the peak stress. Following their approach, we fitted the peak stress data for saturated samples of EB_I (Figure 12a) and EB_III (Figure 12b) to straight lines and inferred by linear regression the two micromechanical parameters D_o and $K_C/\sqrt{\pi c}$ (Figure 12).

Several features of the inferred micromechanical parameter should be noted. First, D_o values of the EB_I samples are inferred to be lower than that of EB_III. This indicates a positive correlation between the initial damage and preexisting crack porosity (Figures 2a and 2c). Second, the inferred values of $K_C/\sqrt{\pi c}$ are significantly higher than the $K_{IC}/\sqrt{\pi c}$ values, as suggested by *Baud et al.* [2014]. It is also of interest to note that the inferred $K_C/\sqrt{\pi c}$ values of 70 MPa and 82 MPa (Figure 12) are basically in the expected range of 23.9–75.7 MPa that we estimated earlier assuming preexisting crack lengths on the order of 10–100 μm and mineral values of $K_{IC} = 0.3$ MPa $m^{1/2}$. Third, that EB_I has a value of $K_C/\sqrt{\pi c}$ higher than EB_III can be attributed to several factors: shorter preexisting cracks, more complex crack coalescence, and difference in phenocryst content. It is of interest to compare our basalt values with those for other rock types. For various rock types (including granite, sandstone, limestone, gabbro, gneiss, and basalt), values of μ inferred from dilatancy onset and peak stress data are in the range of 0.3–0.7 and D_o in the range of 0.1–0.4 (Figure 12c). The initial damage values of our basalt samples are comparable to Westerly granite and San Marcos gabbro, which have significantly lower porosities (of 1% or less) but numerous preexisting microcracks. Whereas EB_III has a friction coefficient comparable to relatively compact silicate rocks such as Westerly granite and Bentheim sandstone, EB_I has a lower coefficient comparable to more porous rocks such as Berea and Vosges sandstones.

It should be noted that in our sliding wing crack analysis, we have excluded the uniaxial compression tests and considered only the relevant data from triaxial compression tests. Theoretically, the model is applicable to unconfined compression tests as well, and one can use the inferred micromechanical parameters shown in Figure 12 to predict the UCS of our basalt samples, if indeed their failure also hinged on the growth and coalescence of sliding wing cracks. The predicted UCS correspond to the intercepts of the upper straight lines

in Figures 12a and 12b. Alternatively, one can predict the UCS using an analytic expression derived by *Baud et al.* [2014]:

$$\sigma_u = \frac{1.346}{\sqrt{1+\mu^2}-\mu}\ \frac{K_C}{\sqrt{\pi c}}\ D_0^{-0.256} \tag{2}$$

Using either method, one would predict UCS values of 295 MPa and 255 MPa for the saturated EB_I and EB_III samples, respectively, if indeed the brittle failure is solely due to sliding wing cracking. However, the experimental measurements are lower almost by a factor of 2 (Figures 1a and 1c), which implies that significant weakening of the basalt samples had derived from another mechanism, likely pore-emanated cracking as analyzed in the last section.

5.3. Inelastic Compaction and Cataclastic Pore Collapse

We compile in Figure 13 data for the critical stress C^* at the onset of shear-enhanced compaction of four basalts with porosities ranging from 7% to 18%. All the tests were conducted on water-saturated samples. *Loaiza et al.* [2012] conducted a comprehensive investigation of compaction in Azores basalt, and their data map out an approximately elliptical cap in the effective mean stress-differential stress space. In this study we conducted two triaxial compression tests on Reykjanes basalt. Together with two data points of *Adelinet et al.* [2013] at the lower end of effective mean stress, the Reykjanes data map out part of what appears to be an analogous cap. Since the porosity of Azores basalt is more than twice that of Reykjanes basalt, these two data sets suggest that the compactive yield stress of a basalt scales inversely with porosity. However, our data for Etna basalt and those of *Shimada* [2000] for Yakuno basalt show that their yield stresses are significantly higher, even though the two basalts have porosities almost the same as Reykjanes basalt, with the implication that porosity is not the primary control on magnitude of the yield stress.

In a clastic rock such as sandstone, inelastic compaction derives primarily from grain crushing initiated by the stress concentrations at grain contacts, which induce intragranular cracks to radiate in a conical pattern toward the interior of the impinging grains [*Menéndez et al*., 1996]. The laboratory data are in basic agreement with a Hertzian fracture model, which predicts that the yield stress scales inversely with porosity and grain size [*Wong et al*., 1997]. In limestones and tuffs, the mechanism is fundamentally different. Typically inelastic compaction involves pore collapse that first initiates at the larger macropores. Cataclasis and microcracking seem to be the dominant deformation mechanisms in the proximity of a pore that has collapsed. Relatively intense cracking would develop with a concentric halo surrounding the pore, and comminuted fragments may spall and fall into the void. *Zhu et al.* [2010] referred to this process as "cataclastic pore collapse." Based on their microstructural observations in limestones that the cataclasis derives from the propagation and coalescence of cracks emanating from micropores, and treating the limestone as a "dual-porosity" medium made up of macropores and micropores, they developed a micromechanical model which predicts that the compactive yield stress scales inversely with porosity. The yield stress is predicted to depend also on the partitioning between macroporosity and microporosity, micropore size, and fracture toughness.

In Alban Hills tuff, similar partitioning of macroporosity and microporosity was observed by *Zhu et al.* [2011], which motivated them to apply an analogous pore collapse model to analyze shear-enhanced compaction. However, they also noted that in tuff the cataclastic damage in the periphery of macropores seems to also involve wing crack growth from preexisting microcracks and their coalescence. To capture this process, they analyzed a second scenario of the micromechanical model, with a dual-porosity medium made up of macropores and microcracks, in which cataclastic damage near a macropore surface develops according to the sliding wing crack model. *Zhu et al.* [2011] concluded that either of the two scenarios (based on the pore-emanated cracks or sliding wing cracks) is consistent with their mechanical data and microstructural observations on tuff.

Our observations on inelastic compaction in EB_II (Figure 9) indicate that it involves a pore collapse mechanism somewhat analogous to that in limestone and tuff, with one important difference that cracking emanating from the relatively few micropores seems to play a minor role in the development of cataclastic damage on the macropore surfaces. Accordingly, we adopted the second scenario of the cataclastic pore collapse model of *Zhu et al.* [2011] to analyze our basalt data. An externally applied stress field induces local stress concentration at the surface of a macropore, and yielding initiates when the local stresses satisfy a specified failure criterion. Both the Mohr-Coulomb and Drucker-Prager yield criteria were considered. Similar to

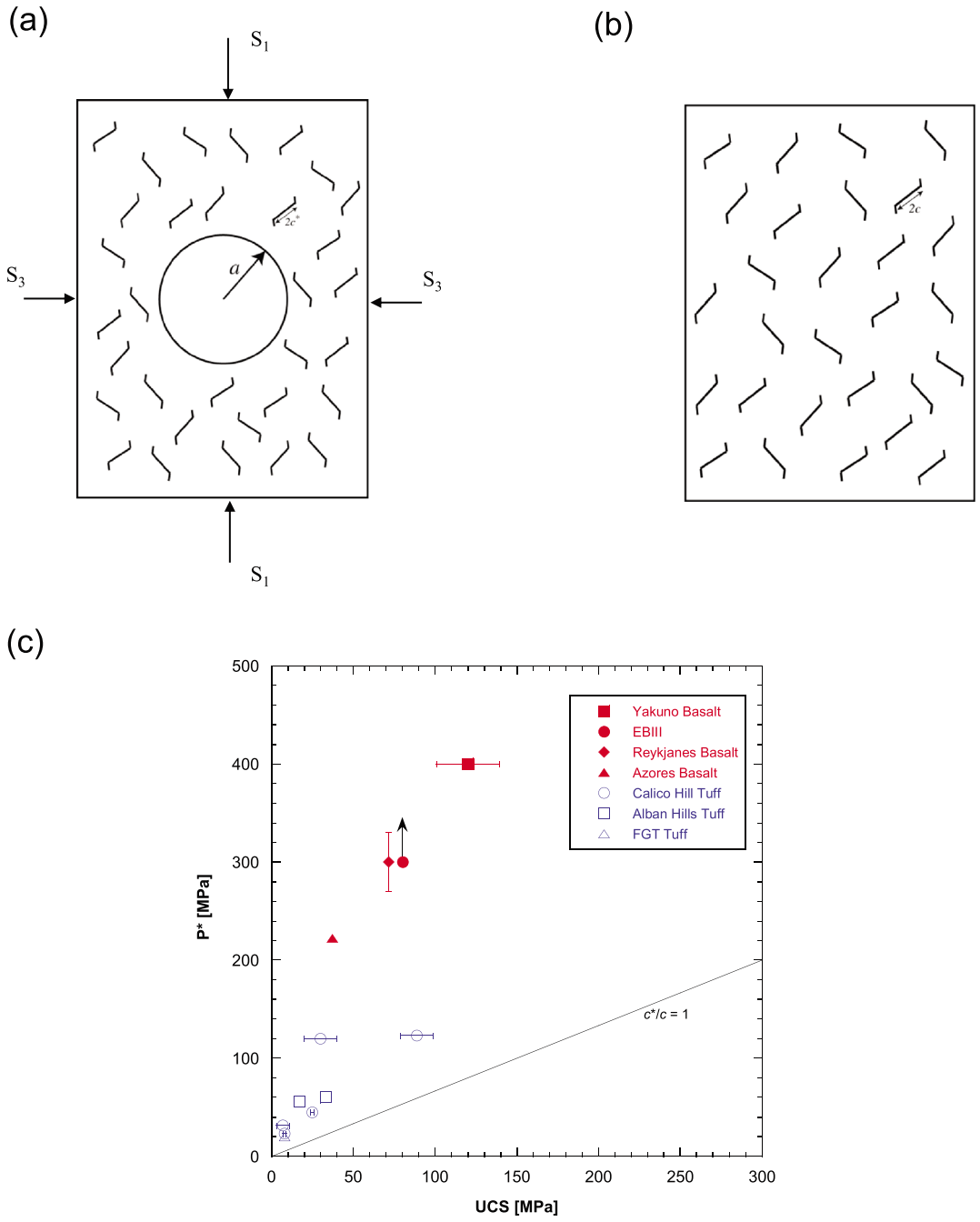

Figure 14. (a) Schematic diagram of a representative volume element. A macropore of radius *a* is surrounded by an effective medium made up of many microcracks with length of 2*c**. (b) A representative volume element of a single porosity medium that numerous preexisting cracks with length of 2*c* are embedded in it. (c) The critical pore collapse pressure *P** is plotted versus the uniaxial compressive strength UCS on EB_II basalt. For comparison, experimental data on Yakuno basalt [*Shimada*, 2000] and Tuffs compiled by *Zhu et al.* [2011] are shown as square symbols. A ratio of *c**/*c* = 1, which correspond to a slope of *P** versus UCS equals 2/3, is plotted in plain line.

previous models of pore collapse [*Bhatt et al.*, 1975; *Gurson*, 1977; *Curran and Carroll*, 1979], the pores are idealized as spherical in shape.

The mechanics of compaction is analyzed with reference to a representative element volume made up of a macropore embedded in cracked medium (Figures 14a and 14b). If we first consider hydrostatic loading, the principal stresses $S_1 = S_2 = S_3 = P_c$ act remotely on the external boundary of the element volume. It can be shown that local stresses in the vicinity of the pore are such that yielding will first occur at the spherical surface (Figure 14a). With reference to a cylindrical coordinate system (ρ, θ, z), the local stresses there are given by

$$\sigma_{\rho\rho} = 0 \tag{3a}$$

$$\sigma_{\theta\theta} = \sigma_{zz} = 3P_c/2 \tag{3b}$$

This stress state corresponds to an "unconfined compression," with a vanishing minimum principal stress. If one adopts the Mohr-Coulomb failure criterion (which is independent of the intermediate principal stress), the failure stress for the stress field (equation (3a)) is identical to that for uniaxial compression. Accordingly, initial yielding (which signals the onset of cataclastic pore collapse) will occur when the maximum principal stress is equal to the UCS σ_u^* of the effective medium:

$$\sigma_{\theta\theta} = \sigma_{zz} = \sigma_u^* \Rightarrow P_c = P^* = 2\sigma_u^*/3 \tag{4}$$

A similar analysis can be performed for the Drucker-Prager criterion, which gives an identical result for a remotely applied hydrostatic loading [*Bhatt et al.*, 1975; *Curran and Carroll*, 1979; *Zhu et al.*, 2010].

In their first analyses *Bhatt et al.* [1975] and *Curran and Carroll* [1979] implicitly assumed that the effective medium has a UCS (and other failure parameters) identical to those of the bulk sample, which would require $\sigma_u^* = \sigma_u$. If indeed this assumption is valid, then equation (4) would imply that a plot of the pore collapse pressure P^* versus the UCS σ_u of the bulk sample falls on a linear trend with a slope of 2/3. We compile in Figure 14c data for four basalts. The EB_II data point is from this study. For the Reykjanes basalt, we measured the UCS under wet condition and estimated P^* to be ~300 MPa from extrapolation of the cap in Figure 13. For the Azores basalt, we measured the UCS and used the P^* data measured by *Loaiza et al.*, [2012]. It can be seen that the basalt above the solid line (with slope 2/3), which implies that $P^* = 2\sigma_u^*/3 > 2\sigma_u/3$, and therefore $\sigma_u^* > \sigma_u$ (Figure 14c). In other words, the effective medium is inferred to have a UCS that is much higher than that of the bulk sample. A similar conclusion applies to data of *Zhu et al.* [2011] for three tuffs (Figure 14c).

In the context of Etna basalt, at least two factors contribute to this discrepancy. First, our observations indicate fundamentally different failure mechanisms on the two different scales. In the bulk sample, uniaxial compressive failure involves pore-emanated cracking. In contrast, the cataclastic damage in the periphery of a macropore seems to be related to wing crack growth and coalescence. Second, the preexisting crack density and/or length may be different on the two different scales. Given these differences we may modify the analytic approximation (2) to apply to the effective medium:

$$\sigma_u^* = \frac{1.346}{\sqrt{1+\mu^2}-\mu}\,\frac{K_C}{\sqrt{\pi c^*}}\left(D_o^*\right)^{-0.256} \tag{5a}$$

where the asterisked quantities are for the effective medium. Here we have made the plausible assumption that for the two different scales, the friction coefficient and fracture toughness are the same. This would then imply that the strength ratio obeys

$$\frac{\sigma_u^*}{\sigma_u} = \frac{\left(D_o^*/D_o\right)^{-0.256}}{\sqrt{(c^*/c)}} \tag{5b}$$

Noting that in the 2-D sliding wing crack mode, the initial damage $D_o \propto n_A c^2$ [*Ashby and Sammis*, 1990] and making another plausible assumption that the area crack density n_A in the effective medium is comparable to that in the bulk sample, we arrive at the conclusion that the UCS is primarily controlled by the preexisting crack length:

$$\frac{\sigma_u^*}{\sigma_u} = \left(\frac{c}{c^*}\right)^{1.012} \tag{5c}$$

Constraints on this strength ratio can be derived from our mechanical data in conjunction with the pore collapse and sliding wing crack models. We do not have direct measurement of the critical pressure P^*, but

since the porosities of EB_II and Yakuno basalts are similar and their compactive yield stresses relatively consistent, we will assume *Shimada*'s [2000] data for P^* (400 MPa) to apply also to Etna basalt. With reference to the pore collapse model (equation (4)), this implies that $\sigma_u^* = 3P^*/2 \approx 600$ MPa. As discussed in the last section, using micromechanical parameters inferred from the sliding wing crack model (Figure 12), the UCS of the bulk sample is predicted to be $\sigma_u \approx 295$ MPa and 255 MPa for the saturated EB_I and EB_III samples, respectively. We thus infer a ratio of $\sigma_u^*/\sigma_u \approx 2.03$ to 2.35, and according to equation (5b) such an enhancement of the UCS can be attributed to a reduction of crack length of 0.43–0.49. The effective medium surrounding a macrocrack samples a relatively small volume, and it is likely that the average crack lengths are shorter. It should be noted that *Zhu et al.* [2011] have also extended their model to nonhydrostatic loading. However, we do not have enough basalt data for a quantitative comparison with the model prediction in this regime.

5.4. Weakening in the Presence of Water

Previous studies have reached apparently contradictory conclusions regarding water weakening in Etna basalt. Whereas *Heap* [2009] reported significant weakening in uniaxial compression (about 13%), *Fortin et al.* [2010] observed almost negligible effect under confinement. Our new data on EB_I together with the uniaxial data of *Heap* [2009] have revealed consistent weakening behavior in Etna basalt under uniaxial and triaxial compression (Figure 3). We also measured the UCS of Reykjanes basalt in dry and wet conditions to be 86 and 72 MPa, corresponding to weakening of 15% (Table 1).

Water weakening has also been reported for sandstone [*Chester and Logan*, 1986; *Rutter and Mainprice,* 1978; *Baud et al*., 2000, 2015], granite [*Hadizadeh and Law*, 1991], porous carbonates [*Baud et al*., 2009], and tuff [*Zhu et al*., 2011]. Overall, the water-weakening effect in basalt seems to be smaller than sandstones. In a recent compilation, *Zhu et al.* [2011] showed that the effect can be up to 50% in sandstone and 80% in tuff.

Previous studies [*Brace and Martin*, 1968; *Duda and Renner*, 2013] showed that beyond a critical strain rate, deformation in saturated rocks could occur too fast to maintain effective drainage. As mentioned in section 3.1, the coincidence of our hydrostatic and triaxial data (Figures 2a and 2c) showed that dilatancy hardening did not contribute to the observed effect of water. *Baud et al.* [2000] interpreted the weakening in the presence of water in sandstone as mostly due to a reduction of the specific surface energy (and of the fracture toughness) and also to the reduction of friction coefficient. With reference to the Hertzian fracture and sliding wing crack models, they analyzed the water-weakening effect in the brittle faulting and cataclastic flow regimes, respectively. Our data here are primarily relevant to the former regime, with the uniaxial compression tests showing well-defined trends of water weakening. However, our observations indicate pore-emanated cracking to be the dominant micromechanical process, and we thus address the question to what extent the results of *Baud et al.* [2000] developed for the sliding wing crack model is applicable here.

It turns out that the result for the pore-emanated crack model is simpler, in that the weakening has no dependence on the friction coefficient. If $K_{IC}^{'}$ denotes the fracture toughness in the presence of water, the ratio between the UCS in wet and dry conditions is given from equation (1) by

$$\frac{\sigma_u^{\text{wet}}}{\sigma_u^{\text{dry}}} \sim \frac{K_{IC}^{'}}{K_{IC}} \tag{6}$$

That the weakening effect in basalt is smaller than sandstone may be due to a smaller reduction of surface energy in the presence of water for minerals such as pyroxene or olivine, which are not found in a sandstone.

6. Conclusions

We investigated the micromechanics of deformation and failure in basalt, focusing on core samples from Mount Etna. Our observations on undeformed samples of porosity ranging from 4 to 16% show the complex microstructure of these volcanic rocks, with pores of various sizes, microcracks, and different proportions of phenocrysts. Dilatancy and brittle faulting were observed in all deformed samples under relatively low effective pressures. Water-saturated samples were weaker than nominally dry samples in this regime. While stress-induced cracking was observed to develop primarily by the reopening of healed and sealed cracks in the low-porosity end-members, pore-emanated microcracking becomes the dominant mechanism of stress-induced damage leading to brittle faulting in the more porous basalts. Our new mechanical data for

brittle faulting are therefore in basic agreement with the predictions of the sliding wing crack model of *Ashby and Sammis* [1990] for the low-porosity end members, and with pore-emanated cracking model of *Sammis and Ashby* [1986] for the high-porosity end-members. Our microstructural observations on failed samples also revealed the tendency for cracking to avoid cutting through the phenocrysts, particularly in rocks with higher proportions of them. New uniaxial data on basalts from Etna, Iceland, and Azores suggested that the mineralogical composition cannot be considered as a primary factor controlling the strength of basalt at least at low temperatures and that this is more the porosity and the topology of the pore space (microcracks and/or pores) that primarily control how strong a basalt can be.

Shear-enhanced compaction was observed at effective pressures as low as 80 MPa in samples of Etna basalt of 8% porosity. Microstructural observations revealed that the main micromechanism of inelastic compaction in basalt is cataclastic pore-collapse as it was recently also observed for limestone and tuff. The porous basalts, which also contained microcracks, could therefore be treated as a dual-porosity medium made up of macropores embedded in an effective medium containing preexisting microcracks. Our new data on Etna and Icelandic basalts as well as published data on Azores [*Loaiza et al*., 2012] and Yakuno [*Shimada*, 2000] basalts are in basic agreement with such a micromechanical model.

Acknowledgments
Data will be available on demand. We thank Marie Violay, Jörg Renner, and the Associate Editor for thoughtful comments on the manuscript. We thank Jérôme Fortin and Alexandre Schubnel for kindly providing the samples of Azores and Reykjanes basalts. We are grateful to Jean-Daniel Bernard and Bertrand Renaudié who prepared the samples in Strasbourg. We thank Cecilia Cheung for helping with the experiments on Reykjanes basalt. We are also grateful to Mike Heap, who provided wet and dry uniaxial data on Etna basalt. We thank Jim Quinn at Stony Brook and Andrea Cavallo at INGV Rome for invaluable assistance with SEM microscopy. We have benefited from discussions with Mathilde Adelinet, Emilie Cazes, Jamie Farquharson, and Thierry Reuschlé. The research at Strasbourg and Hong Kong were partially funded by the France-Hong-Kong Collaborative Program Procore 30805 PM and F-CUHK406/13, respectively. Patrick Baud was partially funded by the LABEX G-EAU-THERMIE profonde of the University of Strasbourg.

References

Adelinet, M., J. Fortin, Y. Guéguen, A. Schubnel, and L. Geoffroy (2010), Frequency and fluid effects on elastic properties of basalt: Experimental investigations, *Geophys. Res. Lett.*, *37*, L02303, doi:10.1029/2009GL041660.

Adelinet, M., J. Fortin, A. Schubnel, and Y. Guéguen (2013), Deformation modes in Icelandic basalt: From brittle failure to localized deformation bands, *J. Volcanol. Geotherm. Res.*, *255*, 15–25.

Ashby, M. F., and C. G. Sammis (1990), The damage mechanics of brittle solids in compression, *Pure Appl. Geophys.*, *133*, 489–521.

Ásmundsson, R., et al. (2014), High temperature instruments and methods developed for supercritical geothermal reservoir characterisation and exploitation—The HiTI project, *Geothermal*, *49*, 90–98.

Atkinson, B. K., and P. G. Meredith (1987), Experimental fracture mechanics data for rocks and minerals, in *Fracture Mechanics of Rock*, edited by B. K. Atkinson, pp. 477–525, Academic Press, London.

Baud, P., W. Zhu, and T.-f. Wong (2000), Failure mode and weakening effect of water on sandstone, *J. Geophys. Res.*, *105*, 16,371–16,390, doi:10.1029/2000JB900087.

Baud, P., S. Vinciguerra, C. David, A. Cavallo, E. Walker, and T. Reuschlé (2009), Compaction and failure in high porosity carbonates: Mechanical data and microstructural observations, *Pure Appl. Geophys.*, *166*, 869–898.

Baud, P., T.-f. Wong, and W. Zhu (2014), Effects of porosity and crack density on compressive strength of rocks, *Int. J. Rock Mech. Min. Sci.*, *67*, 202–211.

Baud, P., T. Reuchlé, Y. Ji, C. N. Cheung, and T.-f. Wong (2015), Mechanical compaction and strain localization in Bleurswiller sandstone, *J. Geophys. Res. Solid Earth*, *120*, 6501–6522, doi:10.1002/2015JB012192.

Benson, P. M., B. D. Thompson, P. G. Meredith, S. Vinciguerra, and R. P. Young (2007), Imaging slow failure in triaxially deformed Etna basalt using 3D acoustic-emission location and X-ray computed tomography, *Geophys. Res. Lett.*, *34*, L03303, doi:10.1029/2006GL028721.

Bhatt, J. J., M. M. Carroll, and J. F. Schatz (1975), A spherical model calculation for volumetric response of porous rocks, *J. Appl. Mech.*, *42*, 363–368.

Brace, W. F., and R. G. I. Martin (1968), A test of the law of effective stress for crystalline rocks of low porosity, *Int. J. Rock Mech. Min. Sci.*, *5*, 415–426.

Chester, F. M., and J. M. Logan (1986), Implications for mechanical properties of brittle faults from observations of the Punchbowl fault zone, California, *Pure Appl. Geophys.*, *124*, 79–126.

Curran, J. H., and M. M. Carroll (1979), Shear stress enhancement of void compaction, *J. Geophys. Res.*, *84*, 1105–1112, doi:10.1029/JB084iB03p01105.

Duda, M., and J. Renner (2013), The weakening effect of water on the brittle failure strength of sandstone, *Geophys. J. Int.*, *192*, 1091–1108.

Fortin, J., S. Stanchits, S. Vinciguerra, and Y. Guéguen (2010), Influence of thermal and mechanical cracks on permeability and elastic wave velocities in a basalt from Mt. Etna volcano subjected to elevate pressure, *Tectonophysics*, *503*, 60–74, doi:10.1016/j.tecto.2010.09.028.

Fowler, A. P. G., R. A. Zierenberg, P. Schiffman, N. Marks, and G. O. Friðleifsson (2015), Evolution of fluid-rock interaction in the Reykjanes geothermal system, Iceland: Evidence from Iceland Deep Drilling Project core RN-17B, *J. Volcanol. Geotherm. Res.*, *302*, 47–63.

Gurson, A. L. (1977), Continuum theory of ductile rupture by void nucleation and growth: Part I - Yield criteria and flow rules for porous ductile media, *J. Eng. Mat. Tech.*, *99*, 2–15.

Hadizadeh, J., and R. D. Law (1991), Water weakening of sandstone and quartzite deformed at various stress and stress rates, *Int. J. Rock Mech. Min. Sci*, *28*, 431–439.

Heap, M. J. (2009), Creep: Time-dependent brittle deformation in rocks, Doctorat of Philosophy, University College London, U. K.

Heap, M. J., S. Vinciguerra, and P. G. Meredith (2009), The evolution of elastic moduli with increasing crack damage during cyclic stressing of a basalt from Mt. Etna volcano, *Tectonophysics*, *471*(1-2), 153–160, doi:10.1016/j.tecto.2008.10.004.

Heap, M. J., D. R. Faulkner, P. G. Meredith, and S. Vinciguerra (2010), Elastic moduli evolution and accompanying stress changes with increasing crack damage: Implications for stress changes around fault zones and volcanoes during deformation, *Geophys. J. Int.*, *183*, 225–236, doi:10.1111/j.1365-246X.2010.04726.x.

Heap, M. J., P. Baud, P. G. Meredith, S. Vinciguerra, A. F. Bell, and I. G. Main (2011), Brittle creep in basalt from Mt Etna volcano: Implications for time-dependent volcano deformation, *Earth Planet. Sci. Lett.*, doi:10.1016/j.epsl.2011.04.035.

Heap, M. J., L. Petrakova, Y. Lavallée, P. Baud, N. R. Varley, and D. B. Dingwell (2014), Microstructural controls on the physical and mechanical properties of edifice-forming andesites at Volcan de Colima, Mexico, *J. Geophys. Res. Solid Earth*, *119*, 2925–2963, doi:10.1002/2013JB010521.

Horii, H., and S. Nemat-Nasser (1986), Brittle failure in compression: Splitting, faulting and brittle-ductile transition, *Phil. Trans. R. Soc. London*, *319*, 337–374.

Jiang, Q., X.-t. Feng, Y. H. Hatzor, X.-j. Hao, and S.-j. Li (2014), Mechanical anisotropy of columnar jointed basalts: An example from the Baihetan hydropower station, China, *Eng. Geol.*, *175*, 35–45.

Kemeny, J. M., and N. G. W. Cook (1991), Micromechanics of deformation in rocks, in *Toughening Mechanisms in Quasi-Brittle Materials*, edited by S. P. Shah, pp. 155–188, Klewer Acad, Norwell, Mass.

Khatiwada, M., L. Adam, M. Morrison, and K. van Wijk (2012), A feasibility study of time-lapse seismic monitoring of CO2 sequestration in a layered basalt reservoir, *J. Appl. Geophys.*, *82*, 145–152.

Loaiza, S., J. Fortin, A. Schubnel, Y. Guéguen, S. Vinciguerra, and M. Moreira (2012), Mechanical behavior and localized failure modes in a porous basalt from the Azores, *Geophys. Res. Lett.*, *39*, L19304, doi:10.1029/2012GL053218.

Matter, J. M., W. S. Broecker, M. Stute, S. R. Gislason, E. H. Oelkers, A. Stefánsson, D. Wolff-Boenisch, E. Gunnlaugsson, G. Axelsson, and G. Björnsson (2009), Permanent carbon dioxide storage into basalt: The CarbFix Pilot Project, Iceland, *Energy Procedia*, *1*(1), 3641–3646.

Menéndez, B., W. Zhu, and T.-f. Wong (1996), Micromechanics of brittle faulting and cataclastic flow in Berea sandstone, *J. Struct. Geol.*, *18*, 1–16.

Ólvasdóttir, J., M. S. Andersen, and L. O. Boldreel (2015), Reservoir quality of intrabasalt volcaniclastic units onshore Faroe Islands, North Atlantic Igneous Province, northeast Atlantic, *AAPG Bull.*, *99*(3), 467–497.

Paterson, M. S., and T.-f. Wong (2005), *Experimental Rock Deformation - The Brittle Field*, 2nd ed., pp. 348, Spinger, New York.

Pope, E. C., D. K. Bird, S. Arnorsson, and N. Giroud (2015), Hydrogeology of the Krafla geothermal system, northeast Iceland, *Geofluids*, *16*(1), 175–197.

Rocchi, V., P. R. Sammonds, and P. G. Meredith (2004), Fracturing Etnean and Vesuvian rocks at high temperature and low pressures, *J. Volcanol. Geotherm. Res.*, *132*, 137–157.

Rutter, E. H., and D. H. Mainprice (1978), The effect of water on stress relaxation of faulted and unfaulted sandstone, *Pure Appl. Geophys.*, *116*, 634–654.

Sammis, C. G., and M. F. Ashby (1986), The failure of brittle porous solids under compressive stress states, *Acta Metall.*, *34*, 511–526.

Schaefer, L. N., J. E. Kendrick, T. Oommen, Y. Lavallée, and G. Chigna (2015), Geomechanical rock properties of a basaltic volcano, *Front. Earth Sci.*, *3*, 29, doi:10.3389/feart.2015.00029.

Shimada, M. (2000), *Mechanical Behavior of Rocks Under High Pressure Conditions*, pp. 178, A.A. Balkema, Netherlands.

Stanchits, S., S. Vinciguerra, and G. Dresen (2006), Ultrasonic velocities, acoustic emission characteristics and crack damage of basalt and granite, *Pure Appl. Geophys.*, *163*(5), 975–994, doi:10.1007/s00024-006-0059-5.

Tanguy, J. C., M. Condomines, and G. Kieffer (1997), Evolution of Mount Etna magma: Constraints on the present feeding system and eruptive mechanism, *J. Volcanol. Geotherm. Res.*, *75*, 221–250.

Vajdova, V., P. Baud, and T.-f. Wong (2004), Compaction, dilatancy and failure in porous carbonate rocks, *J. Geophys. Res.*, *109*, B05204, doi:10.1029/2003JB002508.

Vajdova, V., W. Zhu, T.-M. N. Chen, and T.-f. Wong (2010), Micromechanics of brittle faulting and cataclastic flow in Tavel limestone, *J. Struct. Geol.*, *32*(8), 1158–1169.

Vajdova, V., P. Baud, L. Wu, and T.-f. Wong (2012), Micromechanics of inelastic compaction in two allochemical limestones, *J. Struct. Geol.*, *43*, 100–117.

Vinciguerra, S., C. Trovato, P. Meredith, and P. Benson (2005), Relating seismic velocities, thermal cracking and permeability in Mt. Etna and Iceland basalts, *Int. J. Rock Mech. Min.*, *42*(7-8), 900–910, doi:10.1016/j.ijrmms.2005.05.022.

Violay, M., B. Gibert, D. Mainprice, B. Evans, J.-M. Dautriat, P. Azais, and P. Pezard (2012), An experimental study of the brittle-ductile transition of basalt at oceanic crust pressure and temperature conditions, *J. Geophys. Res.*, *117*, B03213, doi:10.1029/2011JB008884.

Violay, M., B. Gibert, D. Mainprice, and J.-P. Burg (2015), Brittle versus ductile deformation as the main control of deep fluid circulation in oceanic crust, *Geophys. Res. Lett.*, *42*, 2767–2773, doi:10.1002/2015GL063437.

Walsh, J. B. (1965), The effects of cracks on the compressibility of rock, *J. Geophys. Res.*, *70*, 381–389, doi:10.1029/JZ070i002p00381.

Wong, T.-f., and R. Biegel (1985), Effects of pressure on the micromechanics of faulting in San Marcos gabbro, *J. Struct. Geol.*, *7*(6), 737–749.

Wong, T.-f., C. David, and W. Zhu (1997), The transition from brittle faulting to cataclastic flow in porous sandstones: Mechanical deformation, *J. Geophys. Res.*, *102*, 3009–3025, doi:10.1029/96JB03281.

Wu, C., L. Gu, Z. Zhang, Z. Ren, Z. Chen, and W. Li (2006), Formation mechanisms of hydrocarbon reservoirs associated with volcanic and subvolcanic intrusive rocks: Examples in Mesozoic-Cenozoic basins of eastern China, *AAPG Bull.*, *90*(1), 137–147.

Zhu, W., P. Baud, and T.-f. Wong (2010), Micromechanics of cataclastic pore collapse in limestone, *J. Geophys. Res.*, *115*, B04405, doi:10.1029/2009JB006610.

Zhu, W., P. Baud, S. Vinciguerra, and T.-f. Wong (2011), Micromechanics of brittle faulting and cataclastic flow in Alban Hills Tuff, *J. Geophys. Res.*, *106*, B06209, doi:10.1029/2010JB008046.

Zhang, J., T.-f., Wong, and D. M. Davis (1990), High pressure embrittlement and shear-enhanced compaction in Berea sandstone: Acoustic emission measurement and microstructural observation, in *Rock Mechanics Contributions and Challenges, Proceedings of 31st U.S. Symposium on Rock Mechanics*, edited by W. A. Hustrulid, and G. A. Johnson, pp. 653–660, A.A. Balkema, Rotterdam, Netherlands.